bioRxiv preprint doi: https://doi.org/10.1101/2021.10.22.465434; this version posted October 23, 2021. The copyright holder for this preprint (which was not certified by peer review) is the author/funder, who has granted bioRxiv a license to display the preprint in perpetuity. It is made available under aCC-BY 4.0 International license.

Allosteric stabilization of calcium and lipid binding engages three synaptotagmins in fast exocytosis

Janus R. L. Kobbersmed[1,2]*, Manon M. M. Berns[2,3]*, Susanne Ditlevsen[1], Jakob B. Sørensen[2] and Alexander M. Walter[2,3]

[1]Department of Mathematical Sciences, University of Copenhagen, Copenhagen, Denmark

[2]Department of Neuroscience, University of Copenhagen, Copenhagen, Denmark

[3]Molecular and Theoretical Neuroscience, Leibniz-Institut für Molekulare Pharmakologie, FMP im CharitéCrossOver, Berlin, Germany

*: equal contribution

For correspondence:

awalter@sund.ku.dk

Abstract

The release of neurotransmitters from presynaptic terminals is a strongly Ca^{2+}-dependent process controlled by synaptotagmins, especially by their C2B domains. Biochemical measurements have reported Ca^{2+} affinities of synaptotagmin too low to account for synaptic function. However, binding of the C2B domain to the membrane phospholipid $PI(4,5)P_2$ increases the Ca^{2+} affinity and vice versa, indicating a positive allosteric stabilization of simultaneous binding. Here, we construct a mathematical model of the release-triggering mechanism of synaptotagmin based on measured $Ca^{2+}/PI(4,5)P_2$ affinities and reported protein copy numbers. The model reproduced the kinetics of synaptic transmission observed at the calyx of Held over the full range of Ca^{2+} stimuli, with each C2B domain crosslinking Ca^{2+} and $PI(4,5)P_2$ lowering the energy barrier for fusion by 4.85 k_BT. The allosteric stabilization of simultaneous Ca^{2+} and $PI(4,5)P_2$ binding was crucial to form multiple crosslinks which enabled fast fusion rates. Only three crosslinking C2B domains were needed to reproduce physiological responses, but high copy numbers per vesicle sped up the collision-limited formation of crosslinks. *In silico* evaluation of theoretical mutants revealed that affection of the allosteric properties might be a determinant of the severity of synaptotagmin mutations and may underlie dominant-negative, disease-causing effects. We conclude that allostericity is a crucial feature of synaptotagmin action.

bioRxiv preprint doi: https://doi.org/10.1101/2021.10.22.465434; this version posted October 23, 2021. The copyright holder for this preprint (which was not certified by peer review) is the author/funder, who has granted bioRxiv a license to display the preprint in perpetuity. It is made available under aCC-BY 4.0 International license.

Introduction

The release of neurotransmitters (NT) from presynaptic terminals and their subsequent binding to postsynaptic receptors is central to information transfer in chemical synapses. Upon arrival of an action potential (AP) at the presynaptic terminal, voltage-gated Ca^{2+} channels in the active zone (AZ) open. This allows Ca^{2+} influx and causes a brief and local elevation of the intracellular Ca^{2+} concentration ($[Ca^{2+}]_i$). Subsequently, this triggers the fusion of NT-containing synaptic vesicles (SV) from the readily releasable pool (RRP), which is maintained by SV docking and priming, the localization of SVs to the plasma membrane and the molecular maturation to release competence (Kaeser and Regehr, 2017; Sudhof, 2013; Verhage and Sørensen, 2008). The very short temporal profile of the Ca^{2+} signal puts high demands on the Ca^{2+} responsiveness of RRP SVs. Correspondingly, the relationship between presynaptic Ca^{2+} concentration and NT release rates is very steep. Studies have shown a Ca^{2+} cooperativity of 4-5, (Bollmann et al., 2000; Burgalossi et al., 2010; Heidelberger et al., 1994; Schneggenburger and Neher, 2000) and accordingly previous models of NT release have assumed the successive binding of five Ca^{2+} ions to Ca^{2+}-sensitive release machinery (Bollmann *et al.*, 2000; Lou et al., 2005; Schneggenburger and Neher, 2000). However, how this translates to the molecular level is not known.

The energy required for SV fusion is provided by full assembly of the neuronal SNARE complex, which consists of vesicular synaptobrevin and plasma membrane bound SNAP25 and syntaxin (Jahn and Fasshauer, 2012; Sudhof, 2013). SV fusion is coupled to presynaptic elevations of Ca^{2+} concentration by the vesicular Ca^{2+} sensor synaptotagmin (syt) which interacts with the SNAREs (Brewer et al., 2015; Littleton et al., 1993; Mohrmann et al., 2013; Schupp et al., 2016; Zhou et al., 2015; Zhou et al., 2017). Besides a role in fusion, both the SNARE complex and syt are involved in docking and priming of SVs (Chen et al., 2021; Imig et al., 2014; Neher and Brose, 2018; Silva et al., 2021; Walter et al., 2010; Weber et al., 2010).

Several isoforms of syt are expressed in presynaptic terminals. Depending on the synapse type (e.g. hippocampal pyramidal neurons or the Calyx of Held), syt1 or –2 is required for synchronous, Ca^{2+}-induced fusion (Geppert et al., 1994; Kochubey and Schneggenburger, 2011; Sudhof, 2013). The two syt isoforms are highly homologous and contain two cytosolic, Ca^{2+}-binding domains, C2A and –B (Sudhof, 2002), of which the C2B domain has been shown to be essential, and in some case even sufficient, for synchronous NT release (Bacaj et al., 2013; Gruget et al., 2020; Kochubey and Schneggenburger, 2011; Lee et al., 2013; Mackler et al., 2002). The C2B domain contains two Ca^{2+} binding sites on its top loops (Fernandez et al., 2001). In addition, a specific binding site allows C2B to interact with phosphatidylinositol 4,5-phosphate ($PI(4,5)P_2$) in the plasma membrane (Bai et al., 2004; Fernandez-Chacon et al., 2001; Honigmann et al., 2013; Li et al., 2006;

bioRxiv preprint doi: https://doi.org/10.1101/2021.10.22.465434; this version posted October 23, 2021. The copyright holder for this preprint (which was not certified by peer review) is the author/funder, who has granted bioRxiv a license to display the preprint in perpetuity. It is made available under aCC-BY 4.0 International license.

Xue et al., 2008), but might also participate in (possibly transient) SNARE interactions (Brewer *et al.*, 2015; Zhou *et al.*, 2015; Zhou *et al.*, 2017). A third site, located in the far end of the C2B domain and including the two arginines R398 and R399 is also implicated in both SNARE- and membrane contacts (Nyenhuis et al., 2021; Xue *et al.*, 2008; Zhou *et al.*, 2015). The syt C2B domain can induce close membrane-membrane contact *in vitro* (Araç et al., 2006; Chang et al., 2018; Honigmann *et al.*, 2013; Nyenhuis *et al.*, 2021; Seven et al., 2013; Xue *et al.*, 2008), stable vesicle-membrane docking (de Wit et al., 2009), as well as dynamic vesicle-membrane association upon Ca^{2+} influx in the cell (Chang *et al.*, 2018). This is hypothesized to reduce the intermembrane distance below a critical value for SNARE complex assembly and SV fusion (Lin et al., 2014; van den Bogaart et al., 2011b).

Despite its central role as the Ca^{2+} sensor for NT release, the intrinsic Ca^{2+} affinity of the C2B domain is remarkably low (KD ≈ 200 µM, (Radhakrishnan et al., 2009; van den Bogaart et al., 2012)). However, binding of the C2B domain to $PI(4,5)P_2$, which is highly enriched at the AZ, drastically increases its Ca^{2+} affinity. Similarly, the affinity for $PI(4,5)P_2$ increases upon Ca^{2+} binding, indicating positive allosteric coupling between the binding sites of the two species (Li *et al.*, 2006; Radhakrishnan *et al.*, 2009; van den Bogaart *et al.*, 2012). This has been suggested to be due to coulombic (electrostatic) interaction between the two binding pockets (Lin *et al.*, 2014; van den Bogaart *et al.*, 2011b), such that the negative charge of the (unbound) Ca^{2+} binding site lowers the affinity for $PI(4,5)P_2$ until Ca^{2+} binding switches the electrostatic potential. Similarly, the empty $PI(4,5)P_2$ binding site will lower the affinity for Ca^{2+}, until $PI(4,5)P_2$ is bound (Perez-Lara et al., 2016). This arrangement creates a very special situation, where syt is poised to bind to both molecular species - or none of them - but the consequences for the function of syt remain unclear.

Mathematical models provide unique means to combine different sources of experimental information and explore the contribution of different properties to a physiological function. In this paper, we developed a novel stochastic mathematical model in which the allosteric binding of the C2B domain to Ca^{2+} and $PI(4,5)P_2$ is linked to membrane fusion. The model, which is based on the measured affinities and allostericity of Ca^{2+} and $PI(4,5)P_2$ binding, describes stochastic binding/unbinding reactions at the level of each individual syt harbored on a given vesicle, which allows us to explore the relevance of allostericity in the context of the high syt copy number (~15 per vesicle (Takamori et al., 2006)). The model reproduces the steep Ca^{2+} dependency of NT release at the calyx of Held (Kochubey and Schneggenburger, 2011), shows that positive allosteric stabilization is crucial for SV fusion, assigns a relevant role to the syt copy number, and predicts dominant-negative effects of certain syt1 mutations.

bioRxiv preprint doi: https://doi.org/10.1101/2021.10.22.465434; this version posted October 23, 2021. The copyright holder for this preprint (which was not certified by peer review) is the author/funder, who has granted bioRxiv a license to display the preprint in perpetuity. It is made available under aCC-BY 4.0 International license.

Results

An experiment-based model of the triggering mechanism for SV fusion based on molecular interactions between syt, Ca^{2+} and $PI(4,5)P_2$

To investigate the mechanism by which the syt C2B domain, Ca^{2+} and $PI(4,5)P_2$ cooperate to promote SV fusion, we developed an experiment-based model of NT release. In agreement with experimental data (Honigmann *et al.*, 2013; van den Bogaart *et al.*, 2012; Xue *et al.*, 2008), we assume that the two species can bind separately or simultaneously. As the C2B domain binds two Ca^{2+} ions (Fernandez-Chacon *et al.*, 2001; Honigmann *et al.*, 2013; Xue *et al.*, 2008), we assume the cooperative binding of two Ca^{2+} ions to a single C2B domain, which in our model is simplified to a single reaction. Together, this implies that a single C2B domain can be in four different states (Figure 1A): (1) an empty state, (2) a $PI(4,5)P_2$-bound state, (3) a state with two Ca^{2+} ions bound, and (4) a state with both species (Ca^{2+}/$PI(4,5)P_2$) bound. We assume that the simultaneous binding of both Ca^{2+} and $PI(4,5)P_2$ to syt - referred to as crosslinking - promotes SNARE-mediated SV fusion, which is implemented in our model as a lowering of the height of the energy barrier for SV fusion. The increased probability of SV fusion upon formation of a crosslinking syt could, for instance, be mediated by bridging of the plasma and SV membranes by the C2B domain (Figure 1A (Araç *et al.*, 2006; Chang *et al.*, 2018; Honigmann *et al.*, 2013; Lin *et al.*, 2014; Nyenhuis *et al.*, 2021; Nyenhuis et al., 2019; van den Bogaart *et al.*, 2011b)).

The binding affinities of syt1 C2B for Ca^{2+} and $PI(4,5)P_2$ in our model are set to the dissociation constants, $K_{D,2Ca2+}$ and $K_{D,PIP2}$, measured using microscale thermophoresis *in vitro* (van den Bogaart *et al.*, 2012). These experiments revealed that binding of $PI(4,5)P_2$ to the C2B domain increases the domain's affinity for Ca^{2+} and vice versa, indicating positive allosteric coupling between the two binding sites (van den Bogaart *et al.*, 2012). This positive allosteric effect was implemented in the model (illustrated by the red shaded areas of the C2B domain in Figure 1A) by introducing the allosteric factor ($A<1$) on the dissociation rates of Ca^{2+} and $PI(4,5)P_2$ when both species were bound. Based on the Ca^{2+} affinity increase measured *in vitro* by van den Bogaart et al, this value was set to 0.00022 (see Methods)(van den Bogaart *et al.*, 2012). Because closed reaction schemes with no injection of external energy must obey microscopic reversibility (Colquhoun et al., 2004), the same change in $K_{D,PIP2}$ upon binding Ca^{2+} was assumed.

bioRxiv preprint doi: https://doi.org/10.1101/2021.10.22.465434; this version posted October 23, 2021. The copyright holder for this preprint (which was not certified by peer review) is the author/funder, who has granted bioRxiv a license to display the preprint in perpetuity. It is made available under aCC-BY 4.0 International license.

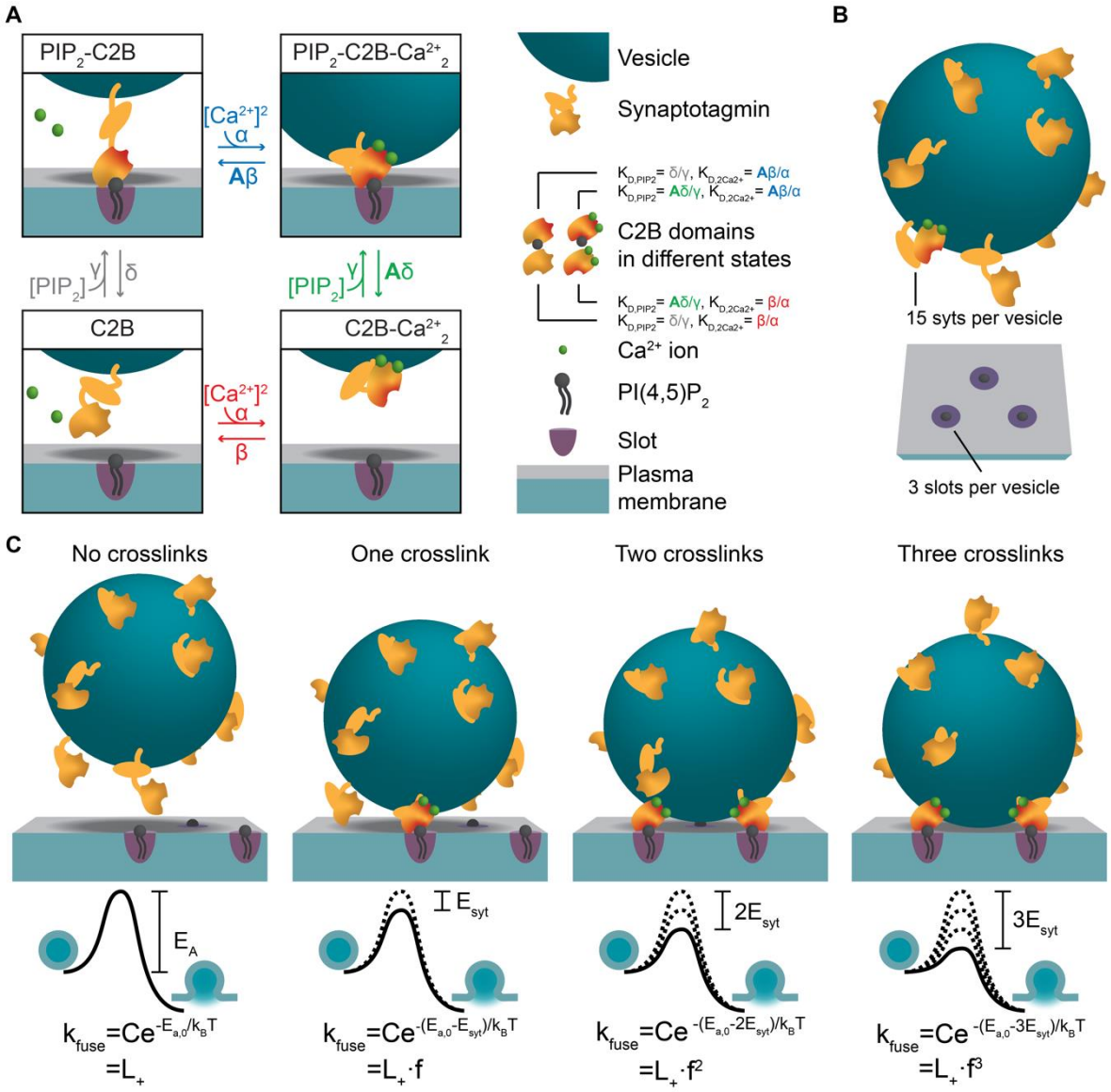

Figure 1: A molecular model of NT release triggered by Ca^{2+} and PI(4,5)P_2 binding to the syt1 C2B domain. A) The reaction scheme of a single syt C2B domain. Each syt can be in one of four binding states: Nothing bound (bottom left), PI(4,5)P_2 bound (top left), two Ca^{2+} ions bound (bottom right), and PI(4,5)P_2 and two Ca^{2+} ions bound (top right). Simultaneous binding of Ca^{2+} and PI(4,5)P_2 to the C2B domain of syt is referred to as crosslinking and might lead to membrane bridging. The factor A<1 on the off-rates (β and δ) from the crosslinked state represents the positive allosteric effect of simultaneous PI(4,5)P_2 and Ca^{2+} binding and leads to stabilization of the crosslinked state. The ratio between off-rate and on-rate constants (β/α and δ/γ) is equal to the respective dissociation constants of syt1 determined *in vitro* ($K_{D,2Ca2+}$ =221^2 μM^2 and $K_{D,PIP2}$ =20μM, (van den Bogaart *et al.*, 2012)) **B)** The stoichiometry at the SV fusion site. We assume 15 syts per SV, and that the association of the syt C2B domain to PI(4,5)P_2-rich patches is limited to a finite number of PI(4,5)P_2 containing slots (here illustrated for M_{slots}=3). **C)** The effect of formation of multiple crosslinks on the distance between the vesicular and plasma membranes, the energy barrier for SV fusion and the SV fusion rate. We assume that each crosslinking C2B domain lowers the energy barrier for fusion by the same amount (E_{syt}, illustrated in middle row), thereby increasing the fusion rate (k_{fuse}) with a factor *f* for each crosslink (equation in bottom row). The model is a Markov model, which can be summarized in a state diagram describing the reactions of the syt-harboring SV (Figure 1 – figure supplement 1). Simulation of the individual syts using the Gillespie algorithm agreed with simulations using the analytical solution of the Markov model (Figure 1 – figure supplement 2 and Methods). Results from simulations using the analytical solution and the Gillespie algorithm can be found in Source data 1 and Simulation scripts can be found in Source code 1 (for Analytica solution) and Source code 2 (for Gillespie algorithm).

bioRxiv preprint doi: https://doi.org/10.1101/2021.10.22.465434; this version posted October 23, 2021. The copyright holder for this preprint (which was not certified by peer review) is the author/funder, who has granted bioRxiv a license to display the preprint in perpetuity. It is made available under aCC-BY 4.0 International license.

It has been estimated that each SV contains 15 copies of syt1 on average (Takamori *et al.*, 2006). We therefore expanded our four-state model (Figure 1A) to a model containing 15 syts per SV (Figure 1B). As the space between the SV and plasma membrane is limited and PI(4,5)P_2 is found in distinct clusters (Honigmann *et al.*, 2013; Milosevic et al., 2005; van den Bogaart et al., 2011a), we considered it unlikely that all 15 syts can bind simultaneously to PI(4,5)P_2 located on the plasma membrane (note that another view holds that 12-20 synaptotagmins form a ring-like assembly (Rothman et al., 2017), but whether they could all bind simultaneously to PI(4,5)P_2 is unclear). Instead, we assume that the number of syts simultaneously engaging with the plasma membrane is limited (constrained to 'slots', Figure 1A-B), which implies that a limited number of syts per SV can simultaneously form crosslinks. We systematically investigated how the number of slots influenced the properties of synaptic exocytosis (see below). In Figure 1, we present a model with three slots per SV, which we found is the minimal number to match physiological responses (see below). We assume that each crosslinking C2B domain lowers the height of the energy barrier for fusion by the same amount, E_{syt}. Because of the exponential relationship between energy barrier height and fusion rate given by the Arrhenius equation, this implies that each crosslink formed increases the fusion rate by the same factor, f (Figure 1C). To account for Ca^{2+}-independent spontaneous release, the fusion rate of an SV with no crosslinks formed was set to $L_+ = 4.23e^{-4}s^{-1}$ (see Methods). Together this gives a total fusion rate of an SV of $k_{fuse}=L_+f^n$, with n being the number of crosslinks formed at this SV, which is equivalent to the release rate function proposed by Lou *et al.* (2005).

The model with 15 syts, (n_{syts} = 15), and an arbitrary (but fixed) number of slots, M_{slots}, is a Markov model, which can be summarized in a state diagram describing the reactions of a single syt-harboring SV (Figure 1 – figure supplement 1). The model was implemented based on the analytical solution, which is ideal for fusion time estimations and fusion rate calculations, as well as with the Gillespie algorithm, which allowed for analyzing stochastic Ca^{2+} and PI(4,5)P_2 binding to the individual syts (Gillespie, 2007). Besides obtaining estimates of average responses, either of the implementations allowed us to estimate the variance predicted by our model (see below and Methods). The two stochastic simulation methods agreed, showing that the Gillespie algorithm yielded precise estimations of the Markov model (Figure 1 - figure supplement 2 and Methods).

At least three crosslinks are required to reproduce release kinetics from the calyx of Held synapse

We aimed to investigate whether our experiment-based model could explain the steep Ca^{2+} dependence of NT release. For this we compared model predictions to exocytosis rates at the entire

bioRxiv preprint doi: https://doi.org/10.1101/2021.10.22.465434; this version posted October 23, 2021. The copyright holder for this preprint (which was not certified by peer review) is the author/funder, who has granted bioRxiv a license to display the preprint in perpetuity. It is made available under aCC-BY 4.0 International license.

range of physiologically relevant $[Ca^{2+}]_i$ measured by Kochubey and Schneggenburger (2011) using Ca^{2+} uncaging experiments at the calyx of Held synapse. The calyx is a well-established model synapse, where NT release is controlled by syt2, which is functionally redundant with syt1 in neurons (Xu et al., 2007). The experimental data consists of release latencies (Figure 2A, top line, defined as the time of the fifth SV fusion after the stimulus) and peak release rates (Figure 2A, bottom line) measured in response to Ca^{2+} uncaging steps. We drove our model with such step-like Ca^{2+} stimuli to predict release latencies and peak release rates (red and blue lines in Figure 2A). To compare model predictions with the experimentally obtained release latencies we derived the likelihood function (see Methods), which quantifies the likelihood of observing the experimental data points, given that the model is true. In other words, the likelihood of release latencies describes how well the model captures the distribution of the experimental release latencies. This approach could not be used for comparison of simulated peak release rates to the experimentally obtained ones, as reliably determining the maximum rate of stochastic simulations is not feasible. Instead, we used the sum of squared deviations to compare analytically obtained model predictions to the experimental data. Both measures of describing the correspondence between model simulations and experimental data were combined in a cost value, which was minimized when fitting the free parameters in our model (see Methods).

Because $K_{D,2Ca2+}$, $K_{D,PIP2}$ and *A* were taken from the literature (Table 1) (van den Bogaart *et al.*, 2012), for each choice of M_{slots} our model only has five free parameters: (1) the binding rate constant of two Ca^{2+} ions, α; (2) the binding rate constant of $PI(4,5)P_2$, γ; (3) the $PI(4,5)P_2$ concentration, $[PI(4,5)P_2]$; (4) the factor on the fusion rate as a result of the reduction of the energy barrier for fusion by each crosslinking syt, $f = e^{E_{syt}/k_B T}$; and (5) an added delay, *d*, which increases the simulated release latencies with a fixed factor over the entire range of $[Ca^{2+}]_i$ and represents Ca^{2+}-independent fusion reactions downstream of Ca^{2+} binding (see (Kochubey and Schneggenburger, 2011; Schneggenburger and Neher, 2000). The size of the RRP was set to an average of 4000 SVs, with a standard deviation (SD) of 2000 (following a gamma distribution) (Figure 2 – figure supplement 1) (Wölfel and Schneggenburger, 2003).

bioRxiv preprint doi: https://doi.org/10.1101/2021.10.22.465434; this version posted October 23, 2021. The copyright holder for this preprint (which was not certified by peer review) is the author/funder, who has granted bioRxiv a license to display the preprint in perpetuity. It is made available under aCC-BY 4.0 International license.

Table 1. Parameters in the model

Parameter	Description	Value
n_{syts}	Number of syts per SV (Takamori *et al.*, 2006)	15
M_{slots}	Number of binding slots for syt to PI(4,5)P2 (see Figure 2)	3
n_{ves}	Number of RRP vesicles (Wölfel and Schneggenburger, 2003)	Mean: 4000, sd: 2000, gamma distribution
Ca_0	Resting $[Ca^{2+}]_i$ (Helmchen et al., 1997)	0.05 µM
$K_{D,2Ca2+}$	Dissociation constant of C2B for two Ca^{2+} ions (van den Bogaart *et al.*, 2012)	221^2 μM^2
$K_{D,PIP2}$	Dissociation constant of C2B for $PI(4,5)P_2$ (van den Bogaart *et al.*, 2012)	20 µM
A	Allosteric factor (van den Bogaart *et al.*, 2012)	0.00022
α	Binding rate constant of C2B for two Ca^{2+} ions (from best fit)	24.70 $\mu M^{-2}s^{-1}$
β	Ca^{2+} unbinding rate constant	$K_{D,2Ca2+} \cdot \alpha$
γ	$PI(4,5)P_2$ binding rate constant of C2B (from best fit)	124.7 $\mu M^{-1}s^{-1}$
δ	$PI(4,5)P_2$ unbinding rate constant of C2B	$K_{D,PIP2} \cdot \gamma$
$[PI(4,5)P_2]$	$PI(4,5)P_2$ concentration (from best fit)	1.109 µM
L_+	Basal fusion rate (computed using data from (Kochubey and Schneggenburger, 2011)	$4.23 \cdot 10^{-4}$ s^{-1}
f	Factor increase in fusion rate upon crosslinking (from best fit)	128.2
Added delay	Value added to the simulated release latencies (from best fit)	0.3803 ms

We first determined whether our model could reproduce the characteristics of Ca^{2+}-dependent NT release and to what extend this was dependent on the number of slots that determine the maximal number of syts per SV simultaneously crosslinking Ca^{2+} and $PI(4,5)P_2$. For this, we optimized the parameters of the model for each choice of M_{slots} from one to six. When including only one slot (M_{slots} =1), the model could explain the experimentally observed release latencies over the full range of tested $[Ca^{2+}]_i$, but failed to reproduce the steep relationship between $[Ca^{2+}]_i$ and peak release rates (Figure 2A). Including more slots strongly improved the agreement between model predictions and experimental data. The best fit was obtained with a model with M_{slots}=3 (Figure 2B). With M_{slots} >3 the agreement between the model and the experimental data reduced slightly, as reflected by increasing cost values (Figure 2B). However, all models with M_{slots}≥3 could describe the steep dependency of peak release rates on $[Ca^{2+}]_i$, with a maximum slope of 4-5 on a double-logarithmic plot (Figure 2C) (Schneggenburger and Neher, 2000). By performing stochastic simulations of the model, it was possible to interrogate from which state the vesicle would fuse. At low $[Ca^{2+}]_i$, SVs mainly fused after one or two syts simultaneously bound Ca^{2+} and $PI(4,5)P_2$ (Figure 2 - figure supplement 2A-C). Interestingly, at moderate to high Ca^{2+} concentrations fusion events primarily took place when three syts simultaneously bound Ca^{2+} and $PI(4,5)P_2$, even when allowing more crosslinking syts (Figure 2D,E, Figure 2 – Figure supplement 2). Correspondingly, the estimated reduction of the energy barrier for fusion contributed by each crosslinking C2B domain was similar for all choices of M_{slots}≥3 (E_{syt}≈4.85k_BT, Figure 2F, see Table 2 for other best fit model parameters). Together, this indicates that

bioRxiv preprint doi: https://doi.org/10.1101/2021.10.22.465434; this version posted October 23, 2021. The copyright holder for this preprint (which was not certified by peer review) is the author/funder, who has granted bioRxiv a license to display the preprint in perpetuity. It is made available under aCC-BY 4.0 International license.

only three syts actively reducing the energy barrier are sufficient for fast SV fusion and M_{slots}=3 was used for further simulations.

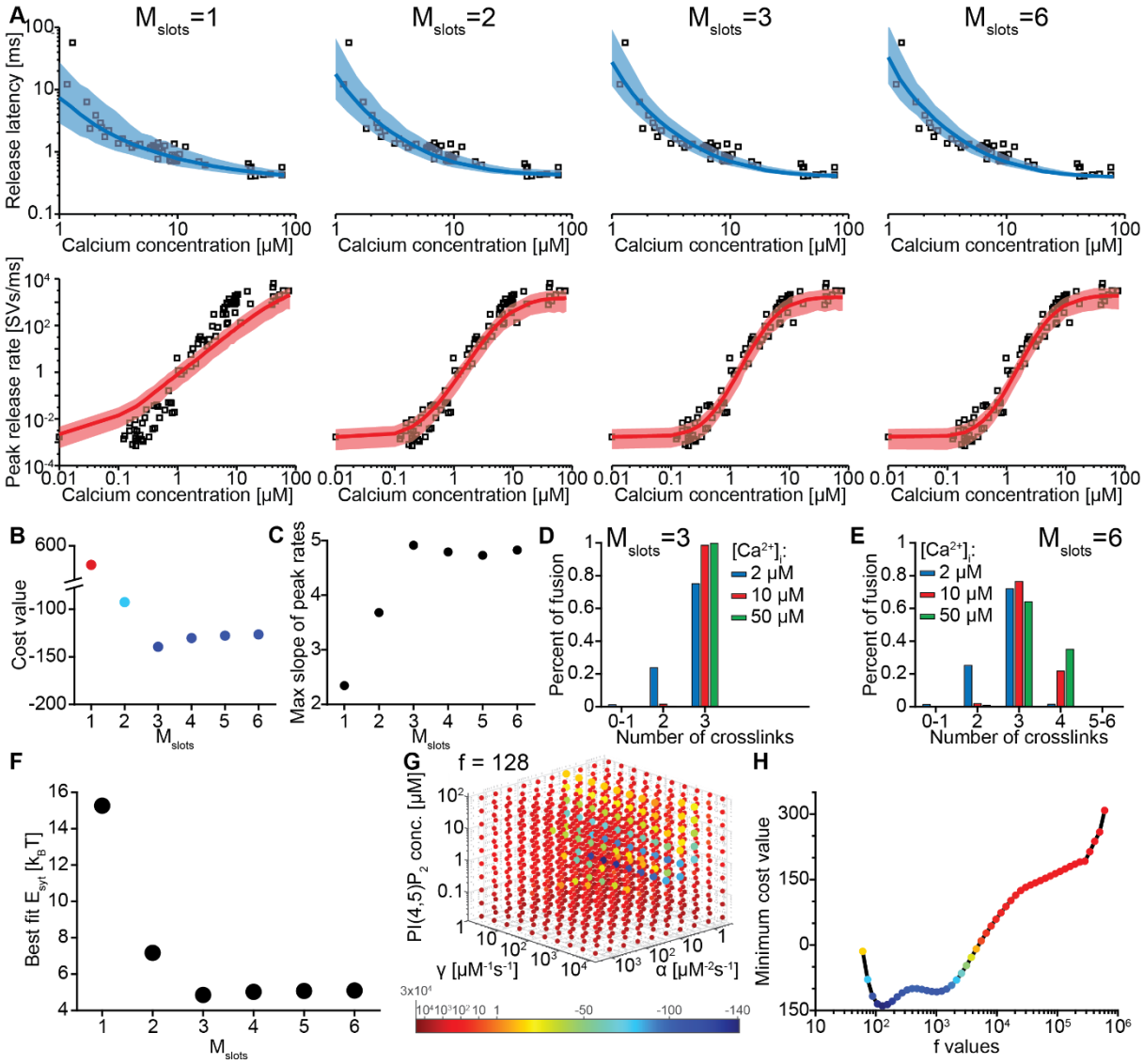

Figure 2: The model reproduces the Ca^{2+} dependency of SV fusion when at least three syts can simultaneously form crosslinks. A) Best fit results for different choices of M_{slots}. The top panels show best fit model prediction of the release latencies (time to fifth SV fusion), and the bottom panels show the predicted peak release rates at varying Ca^{2+} concentrations. The black points are experimental data (individual measurements replotted from Kochubey and Schneggenburger (2011)). Solid lines represent the median release latencies and mean peak release rates predicted by the model from 1000 repetitions per simulated $[Ca^{2+}]_i$. The shaded areas indicate the 95% prediction interval of the model. The models with M_{slots}<3 failed to reproduce data, whereas models with M_{slots}≥3 agreed with data. Optimization and simulation were performed using a variable RRP size (Figure 2 – figure supplement 1). **B)** Minimum cost value as a function of M_{slots}. With M_{slots}=3 the minimum cost value was obtained, indicating the best correspondence to experimental release latencies and peak release rates. The point colors correspond to the color scale in panel G. **C)** Maximal slope of logarithm of simulated peak release rate vs logarithm of $[Ca^{2+}]_i$ on a double-logarithmic plot. For M_{slots}<3 the model failed to reproduce the Ca^{2+} dependency of release rates. **D-E)** The number of crosslinks at the time point of fusion for M_{slots}=3 (D) and M_{slots}=6 (E) determined from simulations of 10^4 SVs using three different $[Ca^{2+}]_i$. Most fusions took place after forming 3 or 4 crosslinks, even when allowing more crosslinks to form. For M_{slots}=6, a larger set of Ca^{2+} concentrations was also explored (Figure 2 – figure supplement 2). **F)** The change in

bioRxiv preprint doi: https://doi.org/10.1101/2021.10.22.465434; this version posted October 23, 2021. The copyright holder for this preprint (which was not certified by peer review) is the author/funder, who has granted bioRxiv a license to display the preprint in perpetuity. It is made available under aCC-BY 4.0 International license.

the energy barrier induced by crosslink formation (E_{syt}) as a function of M_{slots}. E_{syt} was computed from the fitted *f* values and was approximately constant for M_{slots}≥3. **G)** Exploring cost values in the parameter space for a model with M_{slots} =3. With *f* fixed at the best fit value (*f*=128), we determined the cost value of all combinations of 30 choices of the three free parameters, α, γ and [PI(4,5)P_2]. As the added delay only leads to a vertical shift in the release latencies plot (see Figure 2 – figure supplement 3), this parameter was optimized for each choice of the other free parameters to minimize the costs. The plot shows a subset of the parameter combinations, and the colors indicate the cost value at each point. The color scale is linear below 1 and logarithmic above 1, and points with a cost value >1 are smaller for better visibility. The darkest blue colored ball represents the overall minimum cost value in this parameter search and agrees with the best fit obtained. The effect of varying each of the free parameters on release latencies and peak release rates can be seen in Figure 2 – figure supplement 3. **H)** Minimum cost value as a function of *f* for a model with M_{slots} =3. For each choice of *f* the model was fitted. This parameter exploration found the same minimum in the parameter space as found by fitting all free parameters. Simulation scripts can be found in Source code 1. Results from simulations (means and deviations) can be found in Source data 2.

When optimizing a model, there is a risk that the fitted parameters only represent a local minimum in the parameter space or that several sets of parameters fit equally well making the problem ill-posed. To verify that we found optimal parameters for a model with M_{slots}=3, we systematically explored the parameter space by calculating cost values while keeping *f* at its best fit value (*f*=128) and varying the remaining free parameters. This analysis revealed a clear minimum at the best fit parameters (Figure 2G, darkest ball). The isolated effect on the release latencies and peak release rates of each of the five free parameters is shown in Figure 2 - figure supplement 3. In addition, we fitted the model with one less free parameter, keeping the *f* value fixed at different pre-chosen values. The minimum cost value was found with the best fit *f* value (*f*=128) (Figure 2H) and the value of the other parameters agreed with the original best fit. Altogether, despite the low, experimentally observed Ca^{2+} affinities of syt used in our model, it can reproduce synaptic release kinetics measured at the calyx of Held when at least three syts can crosslink Ca^{2+} and PI(4,5)P_2 simultaneously. Moreover, we identified unique parameters for Ca^{2+} and PI(4,5)P_2 binding rates, [PI(4,5)P_2] and the contribution to the energy barrier for fusion provided by a single syt, E_{syt}.

Table 2. Best fit model parameters and corresponding costs with different number of slots

Parameter	**M_{slots} =1**	**M_{slots} =2**	**M_{slots} =3**	**M_{slots} =4**	**M_{slots} =5**	**M_{slots} =6**
α ($\mu M^{-2}s^{-1}$)	0.03712	34.99	24.70	25.08	24.51	24.11
γ ($\mu M^{-1}s^{-1}$)	$1.425e^{5}$	572.6	124.7	121.3	124.31	126.6
[PI(4,5)P_2] (μM)	0.009658	0.2523	1.109	0.4528	0.3048	0.2320
f (E_{syt} (K_bT))	$4.259e^{6}$ (15.3)	1298 (7.17)	128.2 (4.85)	152.1 (5.02)	159.6 (5.07)	163.5 (5.10)
d, added delay (ms)	0.3211	0.3761	0.3803	0.3866	0.3876	0.3881
Costs	581.9	-92.50	-139.4	-130.3	-127.7	-126.5

bioRxiv preprint doi: https://doi.org/10.1101/2021.10.22.465434; this version posted October 23, 2021. The copyright holder for this preprint (which was not certified by peer review) is the author/funder, who has granted bioRxiv a license to display the preprint in perpetuity. It is made available under aCC-BY 4.0 International license.

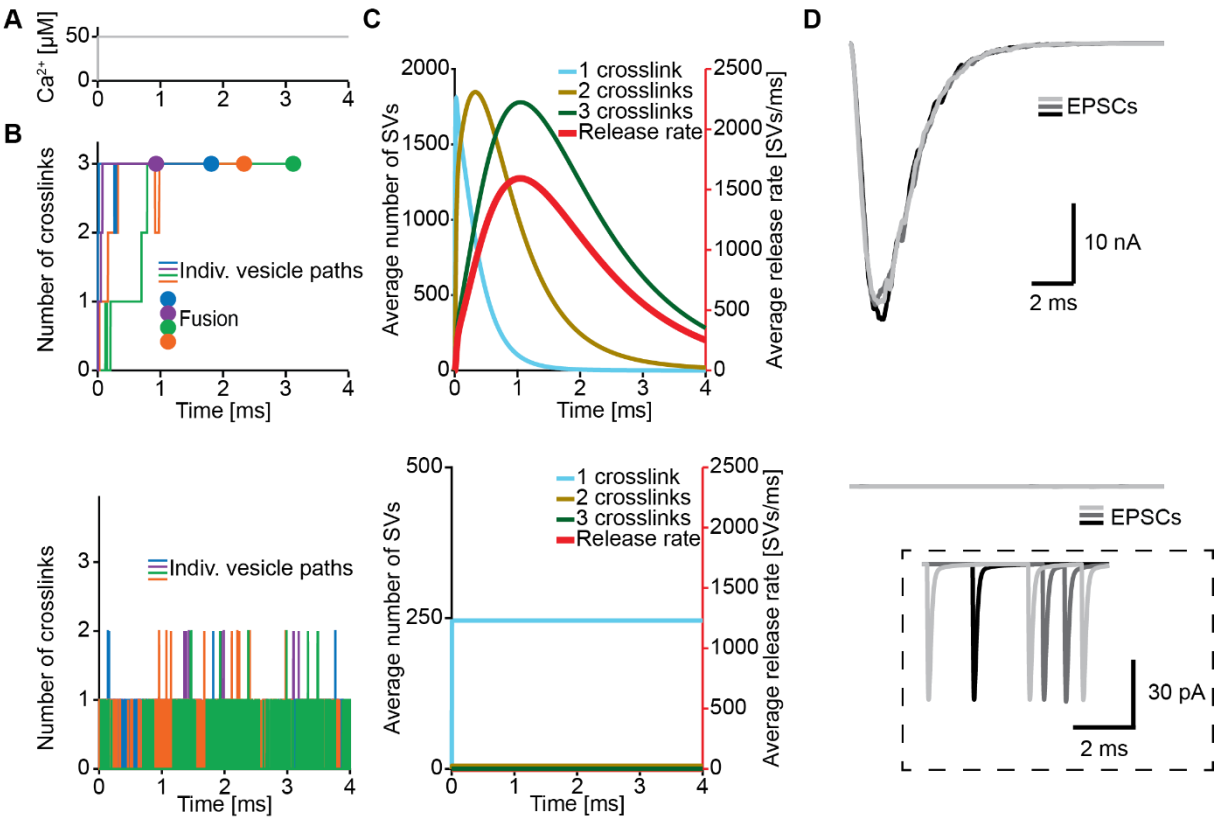

Figure 3: The positive allostericity between Ca^{2+} and $PI(4,5)P_2$ allows multiple crosslink formation. A) Ca^{2+} signal used in simulations of Ca^{2+} uncaging with $[Ca^{2+}]_i$=50 µM. This Ca^{2+} function was used for all simulations depicted in all panels of this figure. **B)** The path towards fusion in the model with (top) and without (bottom) allostericity in stochastic simulation. The different colored graphs show the number of crosslinks over time formed by individual SVs in four example stochastic simulations, and the dots indicate SV fusion. **C)** Average number of SVs having one (blue), two (olive) and three (green) crosslinks formed and the fusion rate (red) over time. With allostericity (top), the number of SVs with three crosslinking syts peaks approximately at the same time as the fusion rate. The decrease in number of SVs with one or two crosslinks reflects formation of additional crosslinks. The decrease in number of SVs is caused by fusion of RRP vesicles. Without allostericity (bottom), almost no SVs form more than one crosslink, which results in a very low fusion rate. **D)** EPSCs from three stochastic simulations and with a fixed RRP size of 4000 SVs. Allostericity ensures synchronous EPSCs (top), while a model lacking this feature only shows sporadic, individual release events (bottom). Insert in the bottom panel shows a zoom-in of the same time interval. Fitting the model without the allosteric effect to the experimental data was unsuccessful (Figure 3 – figure supplement 1). Simulation scripts can be found in Source code 1. Results from fitting the model without allosteric effect can be found in Source data 3.

Allosteric stabilization of Ca^{2+}-induced crosslinking is necessary for multiple crosslink formation and synchronous SV release

To reproduce the steep Ca^{2+} dependency of release, previous models required much higher Ca^{2+} affinities (Bollmann *et al.*, 2000; Burgalossi *et al.*, 2010; Lou *et al.*, 2005; Schneggenburger and Neher, 2000) than the low intrinsic Ca^{2+} affinity of the (non-$PI(4,5)P_2$-bound) C2B domain measured experimentally and used in our model (van den Bogaart *et al.*, 2012). A major difference between these models and ours is the inclusion of the positive allosteric interaction between Ca^{2+} and $PI(4,5)P_2$, which we based on affinity changes observed *in vitro* (van den Bogaart *et al.*, 2012). We

bioRxiv preprint doi: https://doi.org/10.1101/2021.10.22.465434; this version posted October 23, 2021. The copyright holder for this preprint (which was not certified by peer review) is the author/funder, who has granted bioRxiv a license to display the preprint in perpetuity. It is made available under aCC-BY 4.0 International license.

therefore wanted to explore the effects of this property on crosslink formation by investigating the temporal profile of crosslink formation of individual SVs stochastically simulated using our best fit model with (Figure 3A, top) and without (i.e. by setting A=1; Figure 3A, bottom) allosteric coupling. Without positive allosteric coupling, the C2B domain can still bind Ca^{2+} and PI(4,5)P_2 with the measured intrinsic affinity values, but simultaneous binding of both species no longer decreases their unbinding rates. In simulations of the model with allostericity, crosslinks formed faster than they dissolved, leading to the formation of multiple crosslinks per SV (Figure 3A, top). Without the allosteric coupling, crosslinks were not stabilized and they dissolved before additional ones could form. This made it very improbable to reach states with more than one crosslinking syt per SV (Figure 3A, bottom). This is also reflected in the average number of SVs having formed one, two, or three crosslinks (Figure 3B). In the model with allostericity, more and more crosslinks formed over time. After ~1.5 ms, the number of SVs with three crosslinks starts declining because of SV fusion (not crosslink dissociation). The number of SVs with three crosslinks peaked approximately at the same time as the fusion rate (Figure 3B, top), consistent with the observation that most fusion events took place from a state with three crosslinks formed (Figure 2D). Without allostericity, few SVs formed more than one crosslink, resulting in a very low fusion rate (Figure 3B, bottom). Moreover, even if an SV reached a state in which it had formed three crosslinks, the average dissolving time of one of the three crosslinks (~0.0003 ms) was much shorter than the average waiting time for fusion of this SV (~1.1 ms), making SV fusion under these conditions very unlikely. In a model with allostericity, the average waiting time for dissolving one of the three crosslinks (~1.3 ms) exceeds the dwell time before fusion. Thus, the allosteric coupling between Ca^{2+} and PI(4,5)P_2 stabilizes the crosslinked state, thereby ensuring formation of multiple crosslinks per SV and enough dwell time for SV fusion after forming three crosslinks. To investigate the role of allostericity in synaptic transmission we also calculated the Excitatory Postsynaptic Current (EPSC) by convolving fusion times simulated for a Ca^{2+} uncaging stimulus to 50 µM with a miniature EPSC (mEPSC) caused by the release of a single SV (see methods)(Figure 3C). With allostericity, the EPSCs were smooth and synchronous, while removing this feature yielded sporadic, individual release events.

In the above, we explored the consequence of setting A=1 in a model with otherwise unchanged parameters but we also verified the crucial role of the allosteric interaction between Ca^{2+} and PI(4,5)P_2 binding by fitting the model without this property (*A=1*) to the experimental data. With these settings, we could not achieve a satisfactory fit (Figure 3 – figure supplement 1). Similar to the best fit solutions with too few slots (Figure 2A, left), the fitted *f* value was extremely high, which forced very quick SV fusion before the newly formed crosslink dissolved. Thus, when assuming

bioRxiv preprint doi: https://doi.org/10.1101/2021.10.22.465434; this version posted October 23, 2021. The copyright holder for this preprint (which was not certified by peer review) is the author/funder, who has granted bioRxiv a license to display the preprint in perpetuity. It is made available under aCC-BY 4.0 International license.

realistic affinities for Ca^{2+} and $PI(4,5)P_2$, the allosteric property of the syt C2B domain, which leads to a stabilization of the crosslinked state, is necessary to ensure high Ca^{2+} sensitivity of release.

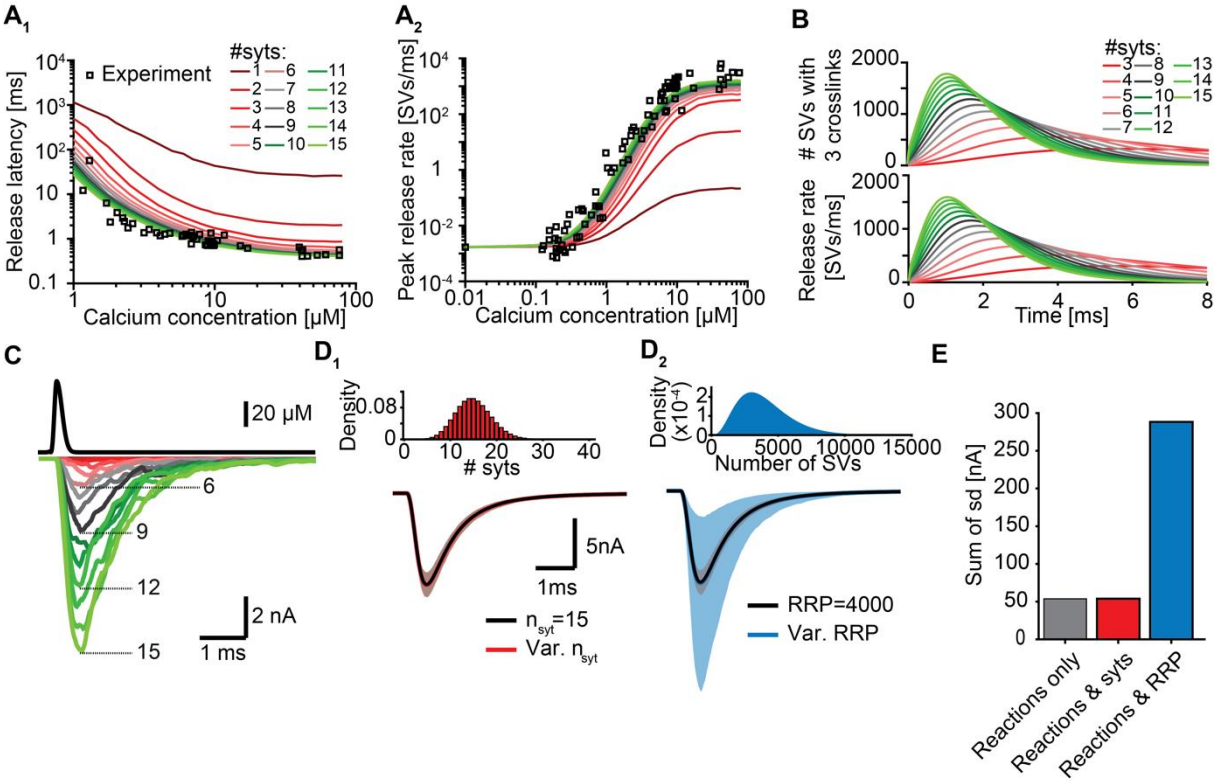

Figure 4: Simulations with reduced syt expression predict a reduction in SV fusion which can be rescued by upregulating [PI(4,5)P_2]. A) Model predictions of median release latencies (A_1) and mean peak release rates (A_2) as a function of $[Ca^{2+}]_i$ for different numbers of syts per SV. All simulations were performed with 1000 repetitions using the best fit parameters obtained by fitting with n_{syts} = 15. Experimental data points are replotted from (Kochubey and Schneggenburger, 2011). **B**) The average number of SVs with three crosslinks formed (top) and release rate (bottom) as a function of time for 3-15 syt copies per SV from simulations with a Ca^{2+} flash of 50 µM. **C)** Predicted AP-evoked responses (bottom) simulated using a realistic Ca^{2+} transient (top) (Wang et al., 2008) for different numbers of syts per SV. The AP-evoked response shown at the bottom are representative single stochastic simulations with an amplitude closest to the mean amplitude of 200 repetitions. Refitting [PI(4,5)P_2] for each choice of $n_{syt} \geq 3$ could fully rescue release latencies, release rates and evoked responses (Figure 4 – figure supplement 1). **D)** Variability in simulated AP-evoked responses for a model with a variable number of syts and an RRP size of 4000 (D_1, red, bottom) and a variable RRP size and 15 syts per SV (D_2, blue, bottom) compared to the variance induced by the stochasticity of the reactions only (with fixed number of SVs and syts, grey). Solid lines depict mean traces and the shaded area indicates the 95% prediction interval. Simulations with 1000 repetitions. Top panels show the probability density distributions of the number of syts (Poisson distribution, lambda =15) and of the number of SVs (gamma distribution, mean =4000 std= 2000). **E)** Quantification of the variance in the traces introduced by the stochasticity of the model reactions (grey), model reactions plus variable syt number (red) and model reactions plus variable RRP size (blue) by computing the sum of the standard deviation determined over the entire trace (0-6 ms, 300 data points). Simulation scripts can be found in Source code 1 (for Figure 4A-B, Figure 4 figure supplement 1A-B) and Source code 2 (for Figure 4C-E, Figure 4 figure supplement 1C-F). Results from simulations (means and deviations) can be found in Source data 4.

High numbers of syts per SV speed up transmission by increasing the probability of crosslink formation

bioRxiv preprint doi: https://doi.org/10.1101/2021.10.22.465434; this version posted October 23, 2021. The copyright holder for this preprint (which was not certified by peer review) is the author/funder, who has granted bioRxiv a license to display the preprint in perpetuity. It is made available under aCC-BY 4.0 International license.

Fitting of the model and the subsequent model evaluation strongly suggest that only three syts simultaneously binding Ca^{2+} and $PI(4,5)P_2$ are required to actively promote SV fusion (Figure 2). Yet, an additional 12 copies are expressed per SV (Takamori *et al.*, 2006), which raises the question why SVs carry such excess of protein and whether all syts present per SV contribute to the characteristics of Ca^{2+}-induced synaptic transmission. To investigate this, we simulated Ca^{2+} uncaging experiments with reduced numbers of syts per SV, while keeping all other parameters in the model constant. Reducing the syt copy number led to an increase in release latencies, which was accompanied by a reduction in peak release rates (Figure 4A). Defects were particularly prominent for reductions to less than three copies per SV (Figure 4A). Further exploration showed that the delay and reduction in transmission were caused by a slowing of the formation of three crosslinks (Figure 4B), consistent with a role of excess syt copies on the vesicle to facilitate multiple crosslink formation for fast fusion.

To investigate the effect of reduced syt copy numbers on SV fusion in a physiologically relevant context, we next simulated AP-evoked EPSCs (eEPSCs) by driving our model with a Ca^{2+} wave describing the time course of $[Ca^{2+}]_i$ sensed locally by RRP SVs in the mouse calyx of Held upon AP stimulation (Wang *et al.*, 2008), Figure 4C, top panel). Like the effect seen with the Ca^{2+}-flash simulations, the simulated eEPSCs showed a reduction in amplitude with decreasing copies of syts per SV (Figure 4C). Removal of a single syt already reduced the average eEPSC amplitude by ~10% and removal of half of its copies reduced the amplitude to only ~25% of the usual amplitude (Figure 4C). These simulations are in line with the reduced NT release upon loss of syt expressed on the SV membrane observed experimentally (Kaempf et al., 2015). (Note, however, that our model only describes the functioning of syt1/2 and therefore does not include other Ca^{2+}-sensors like syt7 and Doc2B, which may mediate release in case of syt1/2 loss (Bacaj *et al.*, 2013; Kochubey et al., 2016; Maximov et al., 2008; Yao et al., 2011)). Taken together, our data show that although only a subset of syts are required to simultaneously bind Ca^{2+} and $PI(4,5)P_2$ to induce fusion, all available syts contribute to the high rates of NT release by increasing the probability of multiple crosslink formation.

Besides high number of syts, the probability of crosslink formation also depends on the $PI(4,5)P_2$ levels. We therefore reasoned that upregulation of $PI(4,5)P_2$ levels could potentially compensate for reduced syt expression. To investigate this, we refitted the model with reduced syt levels to the experimental Ca^{2+} uncaging data (Kochubey and Schneggenburger, 2011) and only allowed $[PI(4,5)P_2]$ to vary. Strikingly, increasing $[PI(4,5)P_2]$ could fully rescue the characteristics of NT release upon reductions in syt levels down to 3 syts per SV (corresponding to an 80% reduction) by reversing the decreased probability of crosslink formation (Figure 4 – figure supplement 1A-C). The required increase in $[PI(4,5)P_2]$ ranged from ~1.1x (14 syts) to ~10x (3 syts, Figure 4 – figure supplement 1D). These elevations also fully restored simulated AP-evoked responses when at least

bioRxiv preprint doi: https://doi.org/10.1101/2021.10.22.465434; this version posted October 23, 2021. The copyright holder for this preprint (which was not certified by peer review) is the author/funder, who has granted bioRxiv a license to display the preprint in perpetuity. It is made available under aCC-BY 4.0 International license.

three syts were present per SV (Figure 4 – figure supplement 1E-F). Altogether these data indicate that upregulating [PI(4,5)P_2] is a potential, powerful compensatory mechanism to rescue reductions of NT release in case the number of syts per SV is reduced which may provide difficulties while evaluating stoichiometric changes experimentally.

As the number of syts per SV had a large impact on the fusion kinetics, we wondered to what extent fluctuations in the number of syts per SV affected the variance in AP-evoked responses. We varied the number of syts expressed per SV following a Poisson distribution with mean =15 (Figure $4D_1$, top panel). Strikingly, varying the number of syts per SV over a large range did not increase the variability in synaptic responses and variance was mainly introduced by fluctuations in RRP size (Figure 4 D,E). This shows that although release kinetics strongly depend on the average number of syt per SV, the system is rather insensitive to fluctuations around this number.

Evaluation of mutants affecting Ca^{2+} binding to the C2B domain reveals diverse effects on AP-evoked transmission

Having developed a mathematical model of syt functioning, we wanted to use its molecular resolution to explore the effects of different mutations in the C2B domain. For that, we designed two different hypothetical Ca^{2+} site mutations. The first mutant, the *"Ca^{2+}-binding"* mutant, had a reduced Ca^{2+} affinity ($10xK_{D,2Ca2+}$) but all other properties were the same as in the WT C2B domain. In the second mutant, we introduced a mutation causing an inability to bind Ca^{2+}. This mutation mimicked the Ca^{2+}-bound state and thereby featured high PI(4,5)P_2 affinity as if the allosteric interaction between Ca^{2+} and PI(4,5)P_2 was permanently in the 'on' state. We termed this mutant the *"no Ca^{2+} binding, A-on"* mutant (Figure 5A). As we explored the significance of the model's stoichiometry (n_{syt}, Figure 4 and M_{slots}, Figure 2) for accurate NT release, we particularly looked into how the stoichiometry of mutant and WT C2B domains affected synaptic transmission by investigating three different conditions (Figure 5B): (1) a homozygous expression condition, (2) a heterozygous expression condition (combined expression of mutant and WT, with a total of 15 syts per SV) and (3) an overexpression condition (expression of mutant together with 15 WT syts per SV). Since most SNAREopathy mutations appear de novo, condition 2 is expected to correspond to most patient conditions (Verhage and Sorensen, 2020), but experimentally, mutations are frequently tested upon overexpression in WT cells (condition 3)(Baker et al., 2018; Bradberry et al., 2020).

Homozygous expression of the *"Ca^{2+}-binding"* mutant generated eEPSCs with a ~50% reduced amplitude and faster kinetics compared to the WT condition (Figure $5C_1$, Figure 5D top). Heterozygous expression only caused a small decrease in mean eEPSC amplitude compared to the expression of 15 WT syts per SV (Figure $5C_1$, Figure 5D middle). Yet, when this mutant was expressed

bioRxiv preprint doi: https://doi.org/10.1101/2021.10.22.465434; this version posted October 23, 2021. The copyright holder for this preprint (which was not certified by peer review) is the author/funder, who has granted bioRxiv a license to display the preprint in perpetuity. It is made available under aCC-BY 4.0 International license.

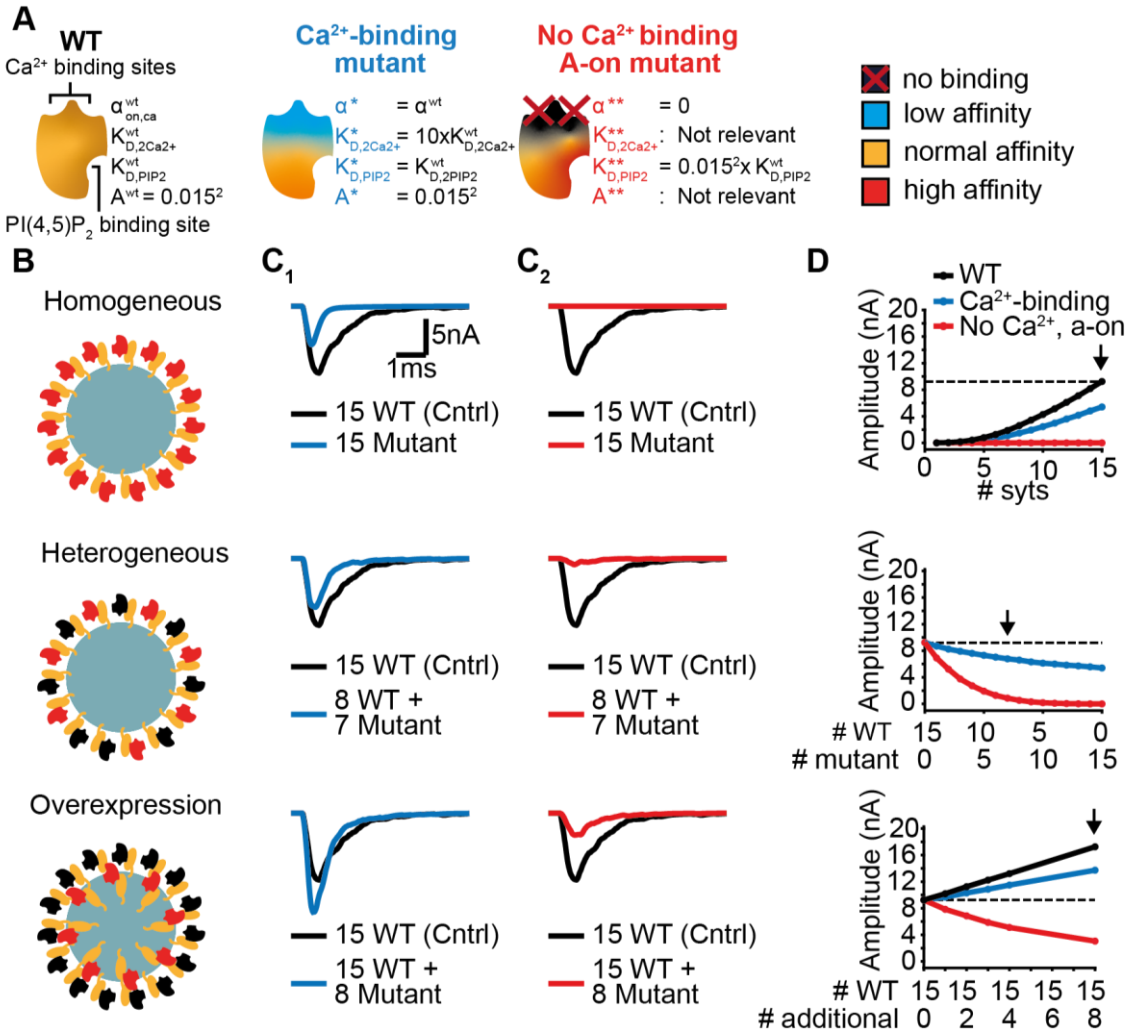

Figure 5: Systematic evaluation of the effect of mutant syts on simulated AP-evoked fusion. A) Illustration of a WT syt and two mutant syts. The *"Ca^{2+}-binding"* mutant has a lower affinity for Ca^{2+} ($K_{D,2Ca2+}$ 10x increased, i.e. β 10x increased). The *"no-Ca^{2+} binding, A-on"* mutant is not able to bind Ca^{2+} and has a high binding affinity for $PI(4,5)P_2$, which is equal to the affinity for $PI(4,5)P_2$ when the allostericity between Ca^{2+} and $PI(4,5)P_2$ is "active" in WT syts (Ca^{2+}-bound state). Because of the inability to bind Ca^{2+}, allosteric interactions between Ca^{2+} and $PI(4,5)P_2$ are not possible in this mutant. **B)** Illustration of homogeneous (top), heterogeneous (middle) and over- expression (bottom) of the mutants. Mutant syts are depicted in red, WT syts are depicted in black. **C)** Representative, stochastically simulated AP-evoked responses with homozygous (top, 15 mutant syt copies), heterozygous (middle, 8 WT and 7 mutant syt copies) and overexpression (bottom, 15 WT and 8 mutant copies of syt) of the different mutants (C_1: *"Ca^{2+}- binding"* mutant, in blue; C_2: *"no Ca^{2+} binding, A-on"* mutant, in red). For each of the settings a representative trace of a condition with 15 WT syts is shown in black (control condition). A third mutation, the *"no Ca^{2+} binding, A-on"* was also explored (Figure 5 – figure supplement 1). **D)** Mean amplitudes of simulated AP-evoked responses (n=200) for the homogeneous (top), heterogeneous (middle) and overexpression (bottom) of the different mutants, and WT (for homozygous and overexpression condition only). Dotted line indicates the mean amplitude of simulated eEPSCs with 15 copies of WT syt (control). Arrow indicates the mutant condition that is depicted in panels C. Increasing the Ca^{2+} influx by prolonging the AP could rescue the *"Ca^{2+}-binding"* mutant but not the *"no Ca^{2+} binding, A-on"* mutant (Figure 5 – figure supplement 2). Simulation scripts can be found in Source code 2. Results from simulations (means and deviations) can be found in Source data 5.

bioRxiv preprint doi: https://doi.org/10.1101/2021.10.22.465434; this version posted October 23, 2021. The copyright holder for this preprint (which was not certified by peer review) is the author/funder, who has granted bioRxiv a license to display the preprint in perpetuity. It is made available under aCC-BY 4.0 International license.

on top of 15 WT syts (overexpression condition), eEPSC amplitudes were increased (Figure 5C$_1$, Figure 5D bottom). The "*no Ca^{2+} binding, A-on*" mutant showed no NT release in response to the Ca^{2+} transient in a homozygous condition (Figure 5C$_2$, Figure 5D top), which is explained by its inability to bind Ca^{2+}. When half of the syts on the SV were mutated (heterozygote) and when this mutant was expressed in a WT background (overexpression), the amplitude of simulated eEPSCs was strongly reduced (Figure 5C$_2$, Figure 5D). Merely four mutant proteins expressed on top of 15 WT proteins already decreased eEPSC amplitudes by 45% (Figure 5D bottom), indicating a strong dominant negative effect. The strong inhibition is a result of the mutant's increased PI(4,5)P_2 affinity leading to "blocking" of PI(4,5)P_2 binding slots on the membrane with a Ca^{2+}-insensitive mutant. In comparison, a mutant not able to bind Ca^{2+} but having a normal PI(4,5)P_2 affinity ("*no Ca^{2+} binding, A-off*" mutant) had a much weaker effect (Figure 5 - figure supplement 1). This indicates that the allosteric interaction between Ca^{2+} and PI(4,5)P_2 plays a prominent role in determining the severity of disease-causing mutations.

It was previously shown that boosting pre-synaptic Ca^{2+} influx by application of 4-Aminopyridine (4-AP), which broadens APs by slowing down the repolarization phase (Alle et al., 2011), could mitigate the effects of heterozygous expression of various syt mutants *in vitro* (Bradberry *et al.*, 2020). We therefore investigated whether the effects of our hypothetical mutants could be reversed by a longer duration of the Ca^{2+} signal. We simulated AP-evoked responses using a Ca^{2+} transient with slower decay kinetics (rise kinetics as the original one, Figure 5 - figure supplement 2A). While this treatment resulted in very little improvement of synaptic responses under expression of the "*no Ca^{2+} binding, A-on*" mutant, it almost fully restored eEPSC amplitudes under heterozygous and homozygous expression of the "*Ca^{2+}-binding*" mutant (Figure 5 - figure supplement 2B-C). Thus, while the two mutations in the C2B domain both reduce synaptic transmission in a heterozygous setting, we show that their treatment requires different strategies. This demonstrates a need for a molecular and functional understanding when developing systematic treatment approaches which can be facilitated by modeling studies as presented here.

bioRxiv preprint doi: https://doi.org/10.1101/2021.10.22.465434; this version posted October 23, 2021. The copyright holder for this preprint (which was not certified by peer review) is the author/funder, who has granted bioRxiv a license to display the preprint in perpetuity. It is made available under aCC-BY 4.0 International license.

Discussion

We here propose a quantitative, experiment-based model describing the function of syt in SV fusion on a molecular level based on biochemical properties determined *in vitro*. In our model, syt acts by lowering the energy barrier for SV fusion by simultaneous binding of Ca^{2+} and $PI(4,5)P_2$ (crosslinking). When allowing at least three crosslinking syts at a time, this model can explain the steep Ca^{2+} dependence of NT release observed at the calyx of Held synapse (Kochubey and Schneggenburger, 2011). Exploring this model led to the following conclusions:

(1) The positive allosteric interaction between Ca^{2+} and $PI(4,5)P_2$ is crucial for fast SV fusion as it stabilizes the crosslinked state to allow multiple crosslinks to form that successively lower the fusion barrier;

(2) At least three syt crosslinks must form to lower the energy barrier for fast SV fusion and to achieve the Ca^{2+} sensitivity inherent to synaptic transmission;

(3) A high copy number of syt ensures high rates of NT release, because it speeds up the formation of three crosslinks;

(4) The molecular resolution of this model can be used to study consequences of disease-causing mutations, which can help elucidate treatment options.

An allosteric interaction between $PI(4,5)P_2$ and Ca^{2+} is crucial for syt1/2 functioning

Our modeling study shows that the biochemically measured allostericity between Ca^{2+} and $PI(4,5)P_2$ (van den Bogaart *et al.*, 2012) is essential for the functioning of syt1/2 in synchronous NT release. Using affinity values of syt for both Ca^{2+} and $PI(4,5)P_2$ obtained in microscale thermophoresis experiments (van den Bogaart *et al.*, 2012), we could only reproduce the steep Ca^{2+} dependency of SV fusion measured at the calyx of Held if this feature was included (Figure 3 – figure supplement 1). With their experiment, van den Bogaart and colleagues (van den Bogaart *et al.*, 2012) determined steady state affinities, which do not provide information on association/dissociation rates. Consequently, it is not known whether allosteric modulation of the C2B domain induces an increase in binding rates or a decrease in unbinding rates of Ca^{2+} and $PI(4,5)P_2$. An increase in Ca^{2+}/$PI(4,5)P_2$ association rates upon allosteric activation would increase the frequency of crosslink formation, but not the duration of the crosslinked state. We here implemented the allosteric interaction as a reduction of the unbinding rates of both Ca^{2+} and $PI(4,5)P_2$ when both species were bound to the C2B domain. Functionally, this implies that the allosteric property of the C2B domain causes a

bioRxiv preprint doi: https://doi.org/10.1101/2021.10.22.465434; this version posted October 23, 2021. The copyright holder for this preprint (which was not certified by peer review) is the author/funder, who has granted bioRxiv a license to display the preprint in perpetuity. It is made available under aCC-BY 4.0 International license.

stabilization of the crosslinked state yielding dwell times long enough to build up multiple crosslinks for fast fusion (Figure 3).

A stabilization of the Ca^{2+}-bound state was also essential to reproduce the Ca^{2+} dependence of release with the previously proposed five-site binding model (Lou *et al.*, 2005), which postulates consecutive binding of five Ca^{2+} ions in SV fusion triggering and has been used by us and others in several studies (Bohme et al., 2016; Kobbersmed et al., 2020; Kochubey and Schneggenburger, 2011; Schotten et al., 2015; Sun et al., 2007; Wolfel et al., 2007). In that model, a correction factor (b<1) was multiplied on the Ca^{2+} dissociation rate, but this factor has not been attributed to a known molecular mechanism. Our model simulations suggest that the allosteric coupling between Ca^{2+} and $PI(4,5)P_2$ binding to the syt C2B domain is the underlying mechanism leading to crosslink stabilization. This property of the C2B domain also explains why its Ca^{2+} binding affinity is low (Radhakrishnan *et al.*, 2009; van den Bogaart *et al.*, 2012) compared to the Ca^{2+} sensitivity of SV fusion (Bollmann *et al.*, 2000; Burgalossi *et al.*, 2010; Schneggenburger and Neher, 2000).

The stoichiometry of the SV fusion machinery

Each SV contains multiple copies of syt (Takamori *et al.*, 2006) which can cooperate in the fusion process. However, the space between the vesicular and plasma membranes is constrained, and $PI(4,5)P_2$ is organized in discrete clusters (Honigmann *et al.*, 2013; Milosevic *et al.*, 2005; van den Bogaart *et al.*, 2011a), making it likely that the number of crosslinking syts is limited. A recently published study of docked SVs using cryo-EM also indicated a limited number of protein complexes between SV and plasma membrane (Radhakrishnan et al., 2021). We here showed that allowing three syts to simultaneously form $PI(4,5)P_2$-Ca^{2+} crosslinks (i.e. M_{slots} = 3) is sufficient to explain the steep Ca^{2+}-dependence of neurotransmitter release (Figure 2 A-C). Moreover, even when allowing more syts to form crosslinks (M_{slots} >3), most fusion events at $[Ca^{2+}]_i$ > 1 μM nonetheless occurred after the formation of three crosslinks (Figure 2 D-E), strongly arguing that no more than three syts are needed for fast vesicle fusion. This prediction matches experimental estimates of the number of SNARE-complexes zippering during fusion (Arancillo et al., 2013; Mohrmann et al., 2010; Shi et al., 2012; Sinha et al., 2011). At lower $[Ca^{2+}]_i$ (0.5-1 μM, Figure 2 - Figure Supplement 2B), the number of crosslinks leading to fusion was reduced (to 1-2). Thus, our model indicates that higher $[Ca^{2+}]_i$ recruits additional syts, thereby speeding up fusion rates, although no cooperative mechanism between syts was included in our model. Instead, higher-order complexes appear via 'kinetic matching' of single complexes forming at the same time, leading to a multiplicative effect on fusion rates. In this aspect, our model is fundamentally different from the suggestion that syts need to preassemble in higher-order rings to execute their function in fusion (Rothman *et al.*, 2017). This difference constitutes the main testable difference between the models; in our model, the function of a single syt is the same,

bioRxiv preprint doi: https://doi.org/10.1101/2021.10.22.465434; this version posted October 23, 2021. The copyright holder for this preprint (which was not certified by peer review) is the author/funder, who has granted bioRxiv a license to display the preprint in perpetuity. It is made available under aCC-BY 4.0 International license.

no matter the number of syts expressed on a vesicle, whereas the obligatory formation of a ring indicates that a cooperative process is needed before syts can execute their function in exocytosis.

Although in our model only three syts can actively contribute to fusion, the model assigns a clear role for the large copy number of syt (15 copies per vesicle on average (Takamori *et al.*, 2006). Synaptic transmission not only depends on syts active during fusion but more copies increase the collision probability of syts with Ca^{2+} and PI(4,5)P_2, and thereby increase the probability of forming multiple crosslinks, which is required for fast synaptic transmission (Figure 4). Correspondingly, aberrant sorting of syts to SVs has shown to affect evoked neurotransmission (Kaempf *et al.*, 2015) and has been linked to disease (Baker *et al.*, 2018; Harper et al., 2020). Thus, increasing the expression level of syts during evolution may have been sufficient to ensure synchronous, reliable NT release. Similarly, high protein abundance might promote other collision-limited processes in fusion of SVs. If in fact SNARE complex assembly occurred downstream of syt crosslink formation (van den Bogaart *et al.*, 2011b) this could give an intuitive explanation for the even higher abundance of synaptobrevin on vesicles (~70 copies (Takamori *et al.*, 2006)), because its collisions with membrane SNAREs would need to occur while syt is crosslinking. Besides increasing syt copy number, the formation of crosslinks could also be promoted by increasing PI(4,5)P_2 levels. Correspondingly, loss of syts could be compensated by upregulation of PI(4,5)P_2 levels (Figure 4 - figure supplement 1). Given that dynamically regulated signaling molecules can compensate for the loss of syts, this puts new demands on experimental procedures when investigating the role of syts and other synaptic proteins using (genetic) perturbations. Although the expression level of syts per SV are tightly regulated (Kaempf *et al.*, 2015; Mutch et al., 2011), it is not unlikely that the number of syts is slightly variable between individual SVs. Strikingly, despite the relevance of the high syt copy number, our model simulations were largely insensitive to heterogeneity in syt copy number between SVs (Figure 4).

Allosteric properties are a critical determinant of the severity of syt mutants

Mutations in the syt C2B domain and in particular its Ca^{2+} binding pockets have been extensively researched (Bacaj et al., 2015; Bradberry *et al.*, 2020; Kochubey and Schneggenburger, 2011; Mackler *et al.*, 2002; Nishiki and Augustine, 2004). Because of the strong positive allosteric coupling between Ca^{2+} and PI(4,5)P_2 binding sites (van den Bogaart *et al.*, 2012), we expect that some of these Ca^{2+} binding site mutations increase the domain's affinity for PI(4,5)P_2 by inducing molecular changes similar to the ones induced by Ca^{2+} binding. Using theoretical and extreme mutants, we here showed that mutations in the Ca^{2+}-binding pocket leading to an increased PI(4,5)P_2 affinity have more severe effects on AP-evoked transmission than those mutations only affecting Ca^{2+} affinity (Figure 5, Figure 5 - figure supplement 1). As the molecular mechanism underlying the allosteric coupling between the Ca^{2+} and PI(4,5)P_2 binding sites of syt remains enigmatic, it is speculative which *real* Ca^{2+}-site

bioRxiv preprint doi: https://doi.org/10.1101/2021.10.22.465434; this version posted October 23, 2021. The copyright holder for this preprint (which was not certified by peer review) is the author/funder, who has granted bioRxiv a license to display the preprint in perpetuity. It is made available under aCC-BY 4.0 International license.

mutations would affect the allosteric properties of the C2B domain. One possible allosteric mechanism involves electrostatic interactions between the negatively charged Ca^{2+} binding pockets and the positively charged $PI(4,5)P_2$ binding site (van den Bogaart *et al.*, 2012). This would imply that mutations altering the charge of the pockets, like the well-known 'DN' mutants (Mackler *et al.*, 2002), could partially trigger the allosteric coupling mechanism and thereby affect $PI(4,5)P_2$ affinity. In turn, mutations altering the size of the pocket without a change in charge, would only affect Ca^{2+} affinity (like in the '*Ca^{2+}-binding*' mutant investigated here, Figure 5). In line with this reasoning and our observation that the mutations affecting the allosteric coupling have more severe dominant-negative effects, a disease-causing mutation neutralizing one of the Ca^{2+}-binding aspartic acids showed a stronger phenotype than a mutation reducing the size of the pocket (Bradberry *et al.*, 2020). Likewise, in *Drosphila*, neutralization of the aspartic acid residues caused a potent dominant-negative effect with decreased apparent Ca^{2+} affinity and close to no NT release (Mackler *et al.*, 2002). Thus, although the mechanisms of the allosteric coupling remain enigmatic, it is likely that this mechanism is a critical determinant for the severity of disease-causing mutations.

Molecular interplay of the release machinery

Syt's actions to promote vesicle fusion are mediated by the SNARE complex, which in our model is implicitly described in the energy provided to lower the fusion barrier. How the syt and the SNARE complex cooperate in the fusion process is not known. One possibility is that fusion is mediated via direct interactions (Zhou *et al.*, 2015). Alternatively – or in addition – the crosslinking syts might promote SNARE-mediated fusion by providing an electrostatic potential for induction of membrane curvature or lipid rearrangement (Araç *et al.*, 2006; Lai et al., 2011; Martens et al., 2007; Ruiter et al., 2019). Furthermore, membrane proximation induced by crosslinking syts (Araç *et al.*, 2006; Chang *et al.*, 2018; Honigmann *et al.*, 2013; Hui et al., 2011; Lin *et al.*, 2014; Nyenhuis *et al.*, 2021; Nyenhuis *et al.*, 2019; Xue *et al.*, 2008) might promote SNRARE-mediated fusion, as shown *in vitro* (Hui *et al.*, 2011). Accordingly, crosslinking syts might reduce the membrane distance below an upper limit for full SNARE complex assembly (Lin *et al.*, 2014; van den Bogaart *et al.*, 2011b). Reduced distances between vesicular and plasma membranes could also promote formation of more crosslinking syts. While it is furthermore possible that the energy provided by each crosslink changes during their successive engagement, we show here that the simplest model (constant and independent contribution) is sufficient to reproduce the biological response.

Besides syt1/2, Munc13 and syt7 have been proposed to function by bridging the vesicular and plasma membranes (Liu et al., 2016; Quade et al., 2019; Tawfik et al., 2021; Voleti et al., 2017). Differences in the distance these bridges may span, the binding rates and affinities for Ca^{2+} and

bioRxiv preprint doi: https://doi.org/10.1101/2021.10.22.465434; this version posted October 23, 2021. The copyright holder for this preprint (which was not certified by peer review) is the author/funder, who has granted bioRxiv a license to display the preprint in perpetuity. It is made available under aCC-BY 4.0 International license.

membranes, which determine the Ca^{2+} sensitivity, duration, speed and sequence of molecular interaction, might explain their diverse roles in SV docking, priming and fusion and versatile effects on spontaneous-, synchronous- and delayed neurotransmission (Augustin et al., 1999; Bacaj *et al.*, 2013; Basu et al., 2007; Liu et al., 2014; Luo and Sudhof, 2017; Quade *et al.*, 2019; Varoqueaux et al., 2002; Vevea et al., 2021; Wen et al., 2010; Xu et al., 2017). Further research will be necessary to gain understanding how these processes shape the energetic landscape of neurotransmitter release. The parrallel extension of models based on molecular interactions such as presented here should allow the recapitulation of more complex synaptic activity patterns relevant for neural processing. Particularly the molecular resolution of such models will be useful to conceptualize the importance of specific molecular interactions for physiological and pathological processes at the synapse.

bioRxiv preprint doi: https://doi.org/10.1101/2021.10.22.465434; this version posted October 23, 2021. The copyright holder for this preprint (which was not certified by peer review) is the author/funder, who has granted bioRxiv a license to display the preprint in perpetuity. It is made available under aCC-BY 4.0 International license.

Materials and Methods

In this paper we propose a model for SV fusion induced by Ca^{2+} and PI(4,5)P_2 binding to n_{syts} syts per SV and with at most M_{slots} syts per SV engaging in PI(4,5)P_2 binding at the same time. We implemented the model in two ways for different simulation purposes: (1) an implementation based on the analytical solution of the model (Matlab procedures for simulation can be found in Source code 1), and (2) an implementation following the Gillespie algorithm (Gillespie, 2007) (Matlab procedures for simulations can be found in Source code 2). In the first implementation we assume a constant $[Ca^{2+}]_i$, (allowing us to simulate Ca^{2+} uncaging experiments), whereas the second version was implemented to allow for $[Ca^{2+}]_i$ to vary over time (allowing us to simulate AP-evoked responses). Another important difference between the two approaches is that the analytical solution describes the binding state of an entire SV and the Gillespie version describes the binding state of each individual syt. Both implementations allow for stochastic evaluation of the model. The first implementation is used in Figure 2, 2 supplement 2, 2 supplement 3, 3, 3 supplement 1, 4A-B and 4 supplement 1A-D. The second implementation is used to simulate the AP-evoked responses and individual SV binding states in Figures 4C-E, 4 supplement 1E-F, 5B-C, and 5 supplements. Consistency between the two approaches was validated by comparison of simulation result distributions in quantile-quantile (Q-Q) plots (Figure 1 – figure supplement 2).

SV states and possible reactions in the analytical version of the model

In the analytical solution of the model, we describe for each SV the number of syts having bound two Ca^{2+} ions, PI(4,5)P_2, or both species. Since syts were assumed to work independently, their order is not relevant, and we therefore do not need to describe the binding state of each individual syt. The possible binding states of an SV are described in Figure 1 – figure supplement 1. Each state is represented by the triplet *(n,m,k)*, with *k* denoting the number syts having bound PI(4,5)P_2, *m* denoting the number of syts having bound two Ca^{2+} ions, and *n* denoting the number of syts having bound both species and thereby having formed a crosslink. n_{syts} is the total number of syts per SV. M_{slots} restricts the number of syts having bound PI(4,5)P_2 simultaneously (this includes syts having bound PI(4,5)P_2 only (*k*), and those having formed a crosslink (*n*). Taken together, this implies that for all states in the model, it holds that

$$k + m + n \leq n_{syts} \text{ and } k + n \leq M_{slots}$$

We numbered the states systematically following a lexicographic ordering, excluding the states that violate the inequalities described above. To illustrate, we write the ordering of all the states *(m,n,k)* with $n_{syts}=3$ and $M_{slots}=2$:

bioRxiv preprint doi: https://doi.org/10.1101/2021.10.22.465434; this version posted October 23, 2021. The copyright holder for this preprint (which was not certified by peer review) is the author/funder, who has granted bioRxiv a license to display the preprint in perpetuity. It is made available under aCC-BY 4.0 International license.

(0,0,0),(0,0,1),(0,0,2),(0,1,0),(0,1,1),(0,1,2),(0,2,0),(0,2,1),(0,3,0),(1,0,0),(1,0,1),(1,1,0),(1,1,1),(1,2,0),(2,0,0),(2,1,0).

Besides these binding states, an additional state, *F*, describes whether the SV has fused. With $n_{syts}=15$ and $M_{slots}=3$, a single SV in our model has 140 + 1 states.

From any state, there are at most 9 possible reactions, one being SV fusion and the other 8 being (un)binding of Ca^{2+} or $PI(4,5)P_2$ to/from a syt. The rates for the possible reactions of a single SV in this model are summarized in Table 3. In many cases, only a subset of the 8 (un)binding reactions are allowed because of the inequalities above (noted under "Condition" in the table).

Table 3. Overview of possible reactions and their rates in the model

Reaction	Condition	Triplet notation	Reaction rate
Binding of $PI(4,5)P_2$ to empty syt	$n+m+k<n_{syts}$ and $n+k<M_{slots}$	(n,m,k)->(n,m,k+1)	$(n_{syts}-n-m-k)(M_{slots}-n-k)[PI(4,5)P_2]\gamma$
Unbinding of $PI(4,5)P_2$	$k>0$	(n,m,k->(n,m,k-1)	$k\delta$
Binding of $Ca^{2+}{}_2$ to empty syt	$n+m+k<n_{syts}$	(n,m,k)->(n,m+1,k)	$(n_{syts}-n-m-k)[Ca^{2+}]^2\alpha$
Unbinding of $Ca^{2+}{}_2$	$m>0$	(n,m,k)->(n,m-1,k)	$m\beta$
Binding of $PI(4,5)P_2$ to form crosslink	$n+k<M_{slots}$ and $m>0$	(n,m,k)->(n+1,m-1,k)	$m(M_{slots}-n-k)[PI(4,5)P_2]\gamma$
Unbinding of $PI(4,5)P_2$ from a crosslink	$n>0$	(n,m,k)->(n-1, m+1,k)	$An\delta$
Binding of $Ca^{2+}{}_2$ to form crosslink	$k>0$	(n,m,k)->(n+1,m,k-1)	$k[Ca^{2+}]^2\alpha$
Unbinding of $Ca^{2+}{}_2$ from a crosslink	n>0	(n,m,k)->(n-1,m,k+1)	$An\beta$
Fusion		(n,m,k)->(F)	L_+f^n

The reaction rates of (un)binding Ca^{2+} or $PI(4,5)P_2$ are calculated as the number of syts available for (un)binding (computed using n_{syts}, n, m, k) times the reaction rate constant (α, β, γ, δ), and, in the case of binding reactions, times the concentration of the ligand ($[PI(4,5)P_2]$ or $[Ca^{2+}]$). We assumed binding of two Ca^{2+} ions to a single C2B domain. In our model this two-step process is simplified to a single reaction step by taking $[Ca^{2+}]_i$ to the power of two. This simplification is valid, because we assumed that syt could only associate to the vesicular membrane when two Ca^{2+} ions are bound, and binding of one Ca^{2+} ion would not induce an 'intermediate' association state to the membrane, nor would it affect the allosteric interaction. To account for the limit on the number of syts bound to

bioRxiv preprint doi: https://doi.org/10.1101/2021.10.22.465434; this version posted October 23, 2021. The copyright holder for this preprint (which was not certified by peer review) is the author/funder, who has granted bioRxiv a license to display the preprint in perpetuity. It is made available under aCC-BY 4.0 International license.

675 PI(4,5)P_2, the number of available, empty slots, (M_{slots}-*n-k),* was multiplied on the PI(4,5)P_2 binding
676 rates. The fusion rate of the SV is computed by $L_+ \cdot f^n$ (similar to (Lou *et al.*, 2005)), with L_+ denoting the
677 basal fusion rate and f the factor of increase in fusion rate by each crosslink being formed. L_+ was set
678 to 4.23e-4 s^{-1} to match the release rate measured at low $[Ca^{2+}]_i$, given an average size of the RRP of
679 4000 SVs (see below).

680 The affinities for Ca^{2+} and PI(4,5)P_2 binding to syt were set to previously determined
681 dissociation constants ($K_{D,Ca2+}=\beta/\alpha=221^2\ \mu M^2$, $K_{D,PI(4,5)P2}=\delta/\gamma=20\ \mu M$) obtained using *in vitro* microscale
682 thermophoresis experiments (van den Bogaart *et al.*, 2012). For determination of the dissociation
683 constant of Ca^{2+}, van den Bogaart and colleagues assumed binding of a single Ca^{2+} ion to the C2AB
684 domain (van den Bogaart et al., 2012). Assuming that in our model the two Ca^{2+} ions bind to the C2B
685 domain with the same affinity, the $K_{D,2Ca2+}$ of the reaction describing binding of two Ca^{2+} ions can be
686 computed from the experimentally derived dissociation constant by taking it to the power of two.
687 This was verified by re-fitting the experimental data with a hill coefficient of 2, which yielded an
688 $K_{D,2Ca2+}$ of ~221^2 (data not shown).

689 The *in vitro* experiments revealed a change in syt1 Ca^{2+} affinity upon binding PI(4,5)P_2, and
690 vice versa (van den Bogaart et al., 2012), indicating a positive allosteric relationship between the two
691 species. We assumed this allosteric effect was due to a stabilization of the crosslinked state by
692 lowering of the unbinding rates of Ca^{2+} and PI(4,5)P_2 with a factor ($A=(3.3/221)^2=0.00022$) and occurs
693 when both species have bound. Upon crosslink formation, both the unbinding rates of Ca^{2+} and
694 PI(4,5)P_2 are multiplied by A, since any closed chemical system must obey microscopic reversibility
695 (Colquhoun *et al.*, 2004). Using the biochemically defined affinities, the number of free parameters in
696 our model was constrained to:

$$\xi = (\alpha, \gamma, [PI(4,5)P_2], f)$$

697 The values of β and δ were determined according to the affinities for each choice of α and γ.

698

699 **The steady state of the system**

700 The steady state of the system before stimulation was determined at a resting, global $[Ca^{2+}]_i$ of 0.05
701 µM (except for simulations with Ca^{2+} levels below this basal value, for those we assumed
702 $[Ca^{2+}]_{rest}=[Ca^{2+}]_i$). To compute the steady state, we assumed that no fusion took place, ignoring the
703 very low fusion rate at resting $[Ca^{2+}]_i$. Under these conditions the model is a closed system of
704 recurrent states and obeys microscopic reversibility, i.e. for every closed loop state diagram, the
705 product of the rate constants around the loop is the same in both directions (Colquhoun *et al.*, 2004).
706 Microscopic reversibility implies detailed balance, meaning that every reaction is in equilibrium at

bioRxiv preprint doi: https://doi.org/10.1101/2021.10.22.465434; this version posted October 23, 2021. The copyright holder for this preprint (which was not certified by peer review) is the author/funder, who has granted bioRxiv a license to display the preprint in perpetuity. It is made available under aCC-BY 4.0 International license.

steady state. Thus, for any two states S_i and S_j which are connected by a reaction, the steady state distribution obeys

$$[S_j] = \frac{r_{ji}}{r_{ij}}[S_i]$$

where $[S_i]$ and $[S_j]$ are steady state quantities and r_{ij} and r_{ji} are the reaction rates between S_i and S_j. Using this property, we calculated the steady state iteratively by setting the population of the first state (state (0,0,0)), equal to 1, and thereafter iteratively computing the states in the order of the state numbering presented above using the following formula's:

$$If\ k > 0: [(n,m,k)] = \frac{r_{k-1,k}}{r_{k,k-1}}[(n,m,k-1)]$$

$$If\ m > 0\ and\ k = 0: [(n,m,0)] = \frac{r_{m-1,m}}{r_{m,m-1}}[(n,m-1,0)]$$

$$If\ n > 0\ and\ m = k = 0: [(n,0,0)] = \frac{r_{n-1,n}}{r_{n,n-1}}[(n-1,0,0)]$$

Afterwards, each state was divided by the sum of all state values and multiplied by the number of SVs in the RRP. In our model simulations, the size of the RRP was variable and followed a gamma distribution with a mean of 4000 SVs and a standard deviation of 2000 SVs, based on experimental estimates from the calyx of Held (Wölfel and Schneggenburger, 2003). In the following calculations we use φ to denote the steady state probability vector (i.e. normalised the sum to 1).

Computation of fusion probabilities and fusion rate

The analytical implementation of our model allowed us to compute the fusion rate and cumulative fusion probabilities with a constant $[Ca^{2+}]_i$ after stimulus onset (t=0), thereby mimicking conditions in Ca^{2+} uncaging experiments. The constant $[Ca^{2+}]_i$ makes the model a homogenous Markov Model. The transition rates of the model can be organized in the intensity matrix, *Q*, such that,

$$Q_{i,j} = k_{i,j}\ for\ i \neq j$$
$$Q_{i,i} = -\sum_{j \neq i} k_{i,j}$$

where $k_{i,j}$ is the rate of the reaction from state *i* to state *j*. Given initial conditions, φ (steady state normalized to a probability vector), free model parameters, ξ, and calcium concentration, *C,*

$$p_{\xi,C}(t) = \varphi \exp(Q_{\xi,C}t)$$

bioRxiv preprint doi: https://doi.org/10.1101/2021.10.22.465434; this version posted October 23, 2021. The copyright holder for this preprint (which was not certified by peer review) is the author/funder, who has granted bioRxiv a license to display the preprint in perpetuity. It is made available under aCC-BY 4.0 International license.

is the distribution of SV states a time t, i.e., a *1* x n_{states} vector with element *i* being the probability of being in state *i* at time point *t*. The single SV cumulative fusion probability is the last element, which we will denote with a subscript F,

$$G_{\xi,C}(t) = \left(p_{\xi,C}(t)\right)_F = \left(\varphi \exp\left(Q_{\xi,C}t\right)\right)_F \quad (1)$$

The fusion rate of a single SV can be calculated directly as the last element of the derivative of (1):

$$G'_{\xi,C}(t) = \left(\frac{dp_{\xi,C}(t)}{dt}\right)_F = \left(\varphi\, Q_{\xi,C} \exp\left(Q_{\xi,C}t\right)\right)_F \quad (2)$$

Multiplying (1) and (2) with the number of SVs yields the cumulative fusion function and fusion rate function, respectively. For simulation of peak release rates and release latencies (in Figure 2-4), we computed (1) and (2) using the best fit parameters from fitting with M_{slots}=3 and n_{syts}=15. This was done for 31 $[Ca^{2+}]_i$ values ranging from 0.001 µM to 80 µM for $t \in [0,100]$ ms with a time step of 0.01 ms (attached data file, "Fusion_calc.mat"). In addition, the functions were calculated in the same way using the best fit parameters for M_{slots}=1,2,4,5,6 with n_{syts}=15 for simulations depicted in Figure 2A-C. In some conditions, especially at low $[Ca^{2+}]_i$, a longer span of the cumulative fusion probability was required and was calculated with the same time step size.

Computation of peak release rates

The peak of the fusion rate can be computed by multiplying the maximum value of the single SV fusion rate function, (2), with n_{ves}. To allow for a variable RRP size, a set of 1000 n_{ves} values were drawn according to the RRP size distribution, the peak release rates were determined, and the mean and 95 % prediction interval determined (Figure 2A, 2 supplement 3, 3 supplement 1, 4A, 4 supplement 1A) for each Ca^{2+} concentration.

For initial parameter exploration (Figure 2G) and for computing the release rates in the fitting routine, it was not feasible to simulate the fusion rate over 100 ms with high temporal precision. Instead, we implemented a custom search algorithm (scripts can be found in accompanying zip-file "Sourcecode1.zip"), which was constructed to shorten calculation time by taking advantage of the release rate function being unimodal. We first found a time point, t_{max}, at which 75-90 % of the SVs had fused. Having computed different time points in the time interval $[0,t_{max}]$, gave us an interval in which the fusion rate showed a local maximum. The algorithm then narrowed the time interval down until a time of peak was found with a precision of 0.01 ms. This method shortened simulation time considerably.

bioRxiv preprint doi: https://doi.org/10.1101/2021.10.22.465434; this version posted October 23, 2021. The copyright holder for this preprint (which was not certified by peer review) is the author/funder, who has granted bioRxiv a license to display the preprint in perpetuity. It is made available under aCC-BY 4.0 International license.

Stochastic simulation of release latencies

Release latencies (Figures 2A, 2 supplement 3, 3 supplement 1, 4A, and 4 supplement 1), which are defined as the time point of the fifth SV fusion event after the onset of simulation, were simulated stochastically by drawing $p_i \in (0,1)$, $i = 1,\ldots,n_{ves}$, from the uniform distribution for each of the 1000 repetitions and each evaluated $[Ca^{2+}]_i$. Each of these random numbers corresponds to the fusion time of an SV, which can be determined using the single SV cumulative fusion probability function (1). To obtain the time point of the fifth SV fusion, the fifth lowest p_i was selected. The corresponding time of fusion was found by interpolation of the single SV cumulative fusion probability, (1). In the corresponding figures, the medians were plotted, since the probability distribution of the release latencies (derived below) was skewed, and the reported data points were single measurements.

Fitting the model to experimental data

We next aimed to fit the model to already published data describing the Ca^{2+}-dependence of NT release in the mouse calyx of Held (Kochubey and Schneggenburger, 2011). The data consist of measurements from Ca^{2+} uncaging experiments, where the release latency, defined as the time point of the fifth SV fusion event, and the peak release rate were estimated at different $[Ca^{2+}]_i$. Besides the four free model parameters, ξ, an additional parameter, *d,* was fitted. *d* is a constant added to the release latencies computed by the model to account for the experimentally observed delay (Kochubey and Schneggenburger, 2011).

The best fit was obtained by minimizing the following cost function:

$$cost_{\xi,d} = 2 \cdot \sum_{i=1}^{n_{,rates}} S_{\xi,i} - \sum_{j=1}^{n_{,latencies}} \ell_{\xi,d,i}$$

where $i=1,\ldots, n_{rates}$ and $j=1,\ldots, n_{latencies}$ are the indices of the experimentally measured $[Ca^{2+}]_i$,

$$S_{\xi,i} = \left(r_{max,model} - r_{max,experiment}\right)^2$$

are the squared deviations of the peak release rates ($1/ms^2$) and ℓ is the logarithm of the likelihood of the release latencies (see derivation below). To combine the two measures of distance between model and experimental data, which are in different units, the squared deviation of the peak release rates was multiplied by a factor 2 before subtracting the logarithm of the likelihood of the release latencies. The cost value was minimized using the inbuilt Matlab function *fminsearch,* which uses a Nelder-Mead simplex method. *fminsearch* was run with different initial parameter values to verify that the global minimum of the cost function was found. During the fitting, the lower and upper

bioRxiv preprint doi: https://doi.org/10.1101/2021.10.22.465434; this version posted October 23, 2021. The copyright holder for this preprint (which was not certified by peer review) is the author/funder, who has granted bioRxiv a license to display the preprint in perpetuity. It is made available under aCC-BY 4.0 International license.

bounds of *d* were set to, respectively, 0.3 ms and 0.405 ms (with the upper bound corresponding to the smallest release latency in the experimental data set). α,γ, and [PI(4,5)P_2] had an upper bound of 10^{10}, and all free parameters needed to be positive. The maximum number of iterations and function evaluations was set to 5000.

The likelihood function of release latencies with fixed RRP size

To fit the model to the experimental release latency measurements, we derived the likelihood function, which is the probability density function of the model for given parameters evaluated at the experimental data points. Thus, optimizing the likelihood function yields parameters for which the data points are most likely if the model is true. We first derive the likelihood of release latency in the case of a fixed RRP size (n_{ves}).

We define the stochastic variable *X*, which describes the stochastic process of the state of a single SV in our model. The fusion time of the SV, τ, is defined as

$$\tau = \inf\{t > 0 | X(t) = F\}$$

where τ itself is a stochastic variable. We define a stochastic vector, *Z*, which consists of all n_{ves} fusion time points in a single experiment. They come from independent, identically distributed stochastic processes with cumulative distribution function $G_{\xi C}(t)$, given in (1). As the release latency is defined as the time of the fifth SV fusion, we order the *Z* variable outcomes ($z_{(1)}, z_{(2)}, \dots, z_{(nves)}$) from first to last fusion time. Using the transformation

$$U_{(i)} = G_{\xi,C}\left(Z_{(i)}\right)$$

we obtain a sequence of stochastic variables, $U_{(i)}$, which are uniformly distributed on the interval (0,1). The ordering is preserved, since $G_{\xi C}(t)$ is monotonely increasing, and *U* has probability density function

$$f_{U_i}(t) = \left|G'_{\xi,C}\left(Z_{(i)}\right)\right|$$

with respect to *t*. $G_{\xi C}'(t) \geq 0$ is given in (2). From order statistics it follows that the kth ordered *U* is beta-distributed with probability density

$$f_{U_{(k)}}(u) = G_{\xi,C}'\left(G_{\xi,C}^{-1}(u)\right) \cdot \frac{n_{ves}!}{(k-1)!\,(n_{ves}-k)!} u^{k-1}(1-u)^{n_{ves}-k}$$

where $u = G_{\xi C}(t)$. Thus, the transformed variable $U_{(k)}$, is beta-distributed, with

$$U_{(k)} \sim \mathrm{Beta}(k, n_{ves} + 1 - k)$$

bioRxiv preprint doi: https://doi.org/10.1101/2021.10.22.465434; this version posted October 23, 2021. The copyright holder for this preprint (which was not certified by peer review) is the author/funder, who has granted bioRxiv a license to display the preprint in perpetuity. It is made available under aCC-BY 4.0 International license.

In the case of the release latency, we are interested in the fifth fusion event (*k=5*). Thus, with a fixed RRP size, the likelihood value for the release latency observations, $T^*=(t^*_1, t^*_2, \ldots, t^*_M)$, at all *M* Ca^{2+} concentrations is

$$\mathcal{L}_\xi(T^*) = \prod_{i=1}^{M} G_{\xi,C_i}{}'(t_i^*)\frac{n_{ves}!}{4!\,(n_{ves}-5)!}G_{\xi,C_i}(t_i^*)^4\left(1-G_{\xi,C_i}(t_i^*)\right)^{n_{ves}-5}$$

In the optimization we minimize minus the log-likelihood:

$$\ell_\xi(T^*) = -\log(\mathcal{L}_\xi(T^*) = -\sum_{i=1}^{M}\left(\log G_{\xi,C_i}{}'(t_i^*)\frac{n_{ves}!}{4!\,(n_{ves}-5)!}G_{\xi,C_i}(t_i^*)^4\left(1-G_{\xi,C_i}(t_i^*)\right)^{n_{ves}-5}\right)$$

which is equivalent to maximizing the likelihood function.

The likelihood of release latencies with variable RRP size

In our model, the RRP size is assumed to follow a Gamma distribution. Let *x* denote the RRP size, $f_{RRP}(x)$ the probability density of the Gamma distribution, and $u= G_{\xi,C}(t)$. The probability density of the release latency at Ca^{2+} concentration C_i is given by

$$\tilde{f}_{U_{(k)}}(u) = \frac{1}{K}\int_5^\infty f_{RRP}(x)\,G_{\xi,C_i}{}'\left(G_{\xi,C_i}^{-1}(u)\right)\cdot\frac{x!}{4!\,(x-5)!}u^4(1-u)^{x-5}dx$$
$$= \frac{G_{\xi,C}{}'\left(G_{\xi,C}^{-1}(u)\right)}{K}\int_5^\infty f_{RRP}(x)\cdot\frac{x(x-1)(x-2)(x-3)(x-4)}{4!}u^4e^{\log(1-u)x}e^{-5\log(1-u)}dx \quad (3)$$

where *K* is a normalization constant, K=1-P(x<5)≈1. The lower limit of the integral reflects that the release latency is only defined when there are more than 5 SVs in the RRP. In simulations this corresponds to redrawing the RRP size whenever an RRP size < 5 SVs occurs, which happens with probability ~3e-11, and is accounted for in the normalization constant K in the following. Inserting the probability density function of a Gamma distribution with shape parameter *k* and scale parameter θ, we get:

$$\tilde{f}_{U_{(k)}}(u) = \frac{G_{\xi,C}{}'\left(G_{\xi,C}^{-1}(u)\right)}{K}\int_5^\infty \frac{1}{\Gamma(k)\theta^k}\cdot x^{k-1}\cdot e^{\frac{-x}{\theta}}$$
$$\cdot\frac{x(x-1)(x-2)(x-3)(x-4)}{4!}u^4e^{\log(1-u)x}e^{-5\log(1-u)}dx$$

We now define the following variables:

$$\tilde{\theta} = \frac{\theta}{1-\theta\log(1-u)}, \qquad a = \frac{u^4e^{-5\log(1-u)}G_{\xi,C}{}'\left(G_{\xi,C}^{-1}(u)\right)}{4!\,(1-\theta\log(1-u))^k} \quad (4)$$

By factoring out and substituting in the above equation we get

bioRxiv preprint doi: https://doi.org/10.1101/2021.10.22.465434; this version posted October 23, 2021. The copyright holder for this preprint (which was not certified by peer review) is the author/funder, who has granted bioRxiv a license to display the preprint in perpetuity. It is made available under aCC-BY 4.0 International license.

$$K\tilde{f}_{U_{(k)}}(u) = \frac{G_{\xi,C}{}'\left(G_{\xi,C}^{-1}(u)\right)u^4 e^{-5(1-u)}}{4!\,(1-\theta\log(1-u))^k}\int_5^\infty \frac{(1-\theta\log(1-u))^k}{\Gamma(k)\theta^k}\cdot x^{k-1}\cdot e^{\frac{-(1-\theta\log(1-u))x}{\theta}}$$
$$\cdot\, x(x-1)(x-2)(x-3)(x-4)dx$$
$$== a\int_5^\infty \frac{1}{\Gamma(k)\tilde{\theta}^k}\cdot x^{k-1}\cdot e^{\frac{-x}{\tilde{\theta}}}\cdot x(x-1)(x-2)(x-3)(x-4)dx \quad (5)$$

Furthermore, we have

$$x(x-1)(x-2)(x-3)(x-4) = x^5 - 10x^4 + 35x^3 - 50x^2 + 24x \quad (6)$$

Since

$$\Gamma(x+1) = x\Gamma(x)$$

we can derive the following useful formula:

$$I_n = \int_5^\infty \frac{1}{\Gamma(k)\tilde{\theta}^k}\cdot x^{k-1}\cdot e^{\frac{-x}{\tilde{\theta}}}\cdot x^n dx$$

$$= \left(\prod_{m=0}^{n-1} k+m\right)\tilde{\theta}^n \int_5^\infty \frac{1}{\Gamma(k+n)\tilde{\theta}^{k+n}}\cdot x^{k+n-1}\cdot e^{\frac{-x}{\tilde{\theta}}}\,dx$$

$$= \left(\prod_{m=0}^{n-1} k+m\right)\tilde{\theta}^n\left(1 - \frac{1}{\Gamma(k+n)}\gamma\left(k+n,\frac{5}{\tilde{\theta}}\right)\right) \quad (7)$$

The third equality follows from the fact that the function in the second integral from above is the probability density function of a gamma distribution with shape parameter *k+n* and scale parameter $\tilde{\theta}$. We therefore replace it with the cumulative distribution function of the gamma distribution, where γ is the lower incomplete gamma function. Combining (4), (5), (6), and (7) yields an explicit expression of the likelihood of a single delay in (3), as

$$\tilde{f}_{U_{(k)}}(u) = \frac{a\cdot(I_5 - 10I_4 + 35I_3 - 50I_2 + 24I_1)}{K}$$

with

$$K = 1 - P(x<5) = 1 - \frac{1}{\Gamma(k)}\gamma\left(k,\frac{5}{\theta}\right)$$

We then minimize the sum of minus the log-likelihoods of the release latency observations.

bioRxiv preprint doi: https://doi.org/10.1101/2021.10.22.465434; this version posted October 23, 2021. The copyright holder for this preprint (which was not certified by peer review) is the author/funder, who has granted bioRxiv a license to display the preprint in perpetuity. It is made available under aCC-BY 4.0 International license.

Syt binding states in the Gillespie simulation of model

In the Gillespie algorithm, the binding state of each individual syt is tracked. The state of the system at time point *t*, *X(t)*, is given by a n_{syt} x n_{ves} matrix. Each element in this matrix describes the binding state of an individual syt using a 2-digit coding system; 00 for no species bound to syt, 01 for PI(4,5)P_2 bound, 10 for two Ca^{2+} ions bound, and 11 for both species bound (crosslinking syt). As with the analytical implementation, each syt can undergo in total 8 different (un)binding reactions (Figure 1A), depending on the binding state of the respective syt. The fusion rate, which depends on the number of crosslinking syts per SV, is determined for the entire SV.

Determining the initial state of the system

The steady state (initial state, *X(0)*) was computed using the same method as described above (see section '*The steady state of the system*') using $[Ca^{2+}]_i$ = 0.05 µM as the resting condition. This resulted in φ, the probability vector of a single SV to be in the different SV-states at steady state. To stochastically determine *X(0)*, we first determined the binding state for each SV, *i.e.* how many crosslinks are formed (*n)* and how many syts have bound Ca^{2+} (*m)* and how many PI(4,5)P_2 (*k)*. For that we drew $p_j \in (0,1)$, $j = 1\ldots,n_{ves}$, from the uniform distribution. The state number of the jth SV, *s*, was determined by:

$$s = \text{smallest integer satisfying } \sum_{i=1}^{s} \varphi_i \geq p_j$$

Via the ordering of states explained above, *s* can be linked to the state triplet (n_s,m_s,k_s). As the order of syts is irrelevant for model simulation, this information on the state of SV_j was transferred to the jth column of the *X(0)* matrix in a systematic way: The first n_s elements were labeled with '11'; elements n_s+1 to n_s+m_s were labeled with '10'; and elements n_s+m_s+1 to $n_s+m_s+k_s$ were labeled with '01', and the remaining elements $(n_s+m_s+k_s+1):n_{syt}$ were set to '00'.

Gillespie algorithm-based simulations of the model

For stochastic evaluation of the model by the Gillespie algorithm (Gillespie, 2007), we next introduced the propensity function *b*, which is defined by:

$b_{i,j}(x)dt :=$ the probability given *(X(t) = X)*, that the ith syt of the jth SV will undergo a reaction in the next infinitesimal time interval [*t, t+dt*].

For element *i,j* in *b*, the total reaction propensity is the sum of propensities of possible reactions given the binding state of the syt and can be computed as follow:

bioRxiv preprint doi: https://doi.org/10.1101/2021.10.22.465434; this version posted October 23, 2021. The copyright holder for this preprint (which was not certified by peer review) is the author/funder, who has granted bioRxiv a license to display the preprint in perpetuity. It is made available under aCC-BY 4.0 International license.

$$b_{i,j}(X_{i,j}) = \begin{cases} \max(M_{slots} - PIP_{tot,j}, 0)\,\gamma\,[PI(4,5)P_2] + \alpha[Ca^{2+}]^2, & X_{i,j} = 00 \\ \delta + \alpha[Ca^{2+}]^2, & X_{i,j} = 01 \\ \beta + \max(M_{slots} - PIP_{tot,j}, 0)\,\gamma\,[PI(4,5)P_2], & X_{i,j} = 10 \\ A\delta + A\beta, & X_{i,j} = 11 \end{cases}$$

with $PIP_{tot,j}$ the total number of syts of SV *j* bound to PI(4,5)P_2. To include the propensity for fusion of an SV, an additional row in *b*, b_f, describes the propensity of fusion for each SV in the matrix;

$$b_{f,j} = l_+ f^{\sum_{i=1}^{n_{syt}} \mathbf{1}_{(X_{i,j}=11)}}$$

This makes *b* a matrix of $(n_{syt}+1) \times n_{ves}$. We denote the sum of all elements in *b* by b_0. Using b_0 and 3 random numbers ($r_n \in (0,1)$, $n = 1,2,3$) drawn from the uniform distribution, we determined the time step to the next reaction and which SV and syt this reaction affects. The time to next reaction, τ, is given by

$$\tau = \frac{1}{b_0} \ln\left(\frac{1}{r_1}\right)$$

since it is exponentially distributed with rate b_0. The index, *j*, of the SV undergoing a reaction is the first index that satisfies:

$$\sum_{j'=1}^{j} \sum_{i=1}^{n_{syt}+1} b_{i,j'} \geq r_2\, b_0$$

Similarly, the index *i* of the syt in SV *j* undergoing a reaction is the smallest integer fulfilling:

$$\sum_{i'=1}^{i} b_{i',j} \geq r_3 \sum_{\hat{\imath}=1}^{n_{syt}+1} b_{\hat{\imath},j}$$

If the row index *i* equals n_{syt}+1, a fusion reaction occurs. The fusion time ($t + \tau$) is saved and all the propensities of SV *j* in *b* are set to 0. If *i* is smaller or equal to n_{syt} a binding or unbinding reaction of one of the two species occurs. To determine which of the four possible reactions is occurring, we define an additional propensity matrix, b_{react}. The first element in b_{react} denotes the propensity of PI(4,5)P_2 binding, the second element the propensity of Ca^{2+} binding, and the third and fourth element the unbinding of PI(4,5)P_2 and Ca^{2+}, respectively. These elements are given by:

$$b_{react,1} = \mathbf{1}_{(X_{i,j}=00 \vee x_{i,j}=10)} \max(M_{slots} - PIP_{tot,j}, 0)\,\gamma\,[PI(4,5)P_2]$$

$$b_{react,2} = \mathbf{1}_{(X_{i,j}=00 \vee X_{i,j}=01)}\, \alpha[Ca^{2+}]^2$$

$$b_{react,3} = \mathbf{1}_{(X_{i,j}=01 \vee X_{i,j}=11)}\, A^{\mathbf{1}_{(X_{i,j}=11)}} \delta$$

bioRxiv preprint doi: https://doi.org/10.1101/2021.10.22.465434; this version posted October 23, 2021. The copyright holder for this preprint (which was not certified by peer review) is the author/funder, who has granted bioRxiv a license to display the preprint in perpetuity. It is made available under aCC-BY 4.0 International license.

$$b_{react,4} = \mathbf{1}_{(X_{i,j}=10 \vee X_{i,j}=11)} A^{\mathbf{1}(X_{i,j}=11)} \beta$$

Additionally, we define the transition matrix *V*, which describes the change in the state of $X_{i,j}$ induced by the four reactions:

$$V = (+01, +10, -01, -10)$$

A fourth random number, $r_4 \in (0,1)$, drawn from the uniform distribution, determines which reaction occurs via:

h = smallest integer satisfying $\sum_{h'=1}^{h} b_{react,h'} \geq r_4 \sum_{\hat{h}=1}^{4} b_{react,\hat{h}}$

The state of the corresponding SV and syt, $X_{i,j,}$ is replaced by $X_{i,j} + V_h$ and t by $t + \tau$. Then *b* is updated according to the change in *X,* and all steps are repeated. This iterative process continues until all SVs are fused, when simulating the model with a fixed $[Ca^{2+}]_i$.

When simulating AP-evoked responses, we used a Ca^{2+} transient describing the microdomain $[Ca^{2+}]_i$ sensed locally by primed SVs in the mouse calyx of Held upon AP stimulation (Wang *et al.*, 2008). Similar to the uncaging simulations, the $[Ca^{2+}]_i$ before the onset of the stimulus was 0.05µM. Since the Ca^{2+} concentration is a factor in the reaction rates, the propensity matrices *b* and b_{react} were not only updated to the new state matrix, $X(t + \tau)$, but also to a new $[Ca^{2+}]_i$ at time $t + \tau$. $[Ca^{2+}]$ at time $t + \tau$ was determined from the Ca^{2+} transient using linear interpolation, and *b* and b_{react} were updated correspondingly. As the propensity of Ca^{2+} binding is largely dependent on $[Ca^{2+}]_i$, the time step between two updates in $[Ca^{2+}]_{curr}$ and the propensity matrices was set to be at most $8e^{-4}$s. If τ determined from *b* at time *t* was larger than this time step, no reaction occurred, but the system and $[Ca^{2+}]_{curr}$ were updated to time t+$8e^{-4}$s. The model was evaluated until the end of the Ca^{2+} transient. Because this approach requires simulation of all individual (un)binding reactions and fusion events it is not feasible to perform 1000 repetitions. Instead, simulations were repeated 200 times. Like with the computation of the release latencies and maximal fusion rates, we assumed a variable RRP. However, instead of drawing random pool sizes from a gamma distribution, we used the 200 quantiles of the pdf of the RRP sizes, because of the limited number of repetitions and the large impact of the RRP size on the model predictions.

Simulating the model with mutant syts

For mutations in syt that affect the binding and unbinding rates of $PI(4,5)P_2$ and Ca^{2+}, the procedure described above was repeated with adjusted parameters when simulating a model containing only mutant syts. For a model in which mutant proteins were expressed together with WT syts

bioRxiv preprint doi: https://doi.org/10.1101/2021.10.22.465434; this version posted October 23, 2021. The copyright holder for this preprint (which was not certified by peer review) is the author/funder, who has granted bioRxiv a license to display the preprint in perpetuity. It is made available under aCC-BY 4.0 International license.

(simulations of heterozygous and overexpression conditions in Figure 5), the procedure was changed slightly.

For a model with *p* WT and *q* mutant syts, the number of states of an SV increases drastically and was now described by six values; the number of WT syts bound to Ca^{2+}, $PI(4,5)P_2$ or both, and the number of mutant syts bound to Ca^{2+}, $PI(4,5)P_2$ or both. The dimensions of the Q-matrix used to compute the steady-state probability of a single SV increased proportionally with n_{states}. *X(t=0)* was computed using the same principle as described above, with the important difference that the first *p* rows represented the binding status of the WT syts, and row *p+1:p+q* that of the mutants. In *b* this ordering of WT and mutant syts is the same. The parameters used to compute b_{react} depended on whether a reaction occurred to a WT syt, $i \leq p$, or a mutant syt, $n_{syt} \geq i > p$.

Simulation of EPSCs

Simulated EPSCs were obtained using both model implementations. The analytical implementation of our model was used to simulate fusion times for a constant $[Ca^{2+}]_i$ (Figure 3D). The Gillespie version of the model was used to simulate AP-evoked EPSCs with or without mutant syts (Figure 4C-E, Figure 4 - figure supplement 1, Figure 5C-D and 5 supplements). In both approaches the stochastically determined fusion times, determined as described above, were rounded up to the next 0.02 ms, leading to a sampling rate of 50 kHz. The sampled fusion times were convolved with a mEPSC to generate simulated EPSCs. The standard mEPSC used for deconvolution followed the equation described by Neher and Sakaba (Neher and Sakaba, 2001):

$$I_{mini}(t) = A \cdot (1-\rho)\exp\left(-\frac{t}{\tau_1}\right) + \rho \cdot \exp\left(-\frac{t}{\tau_2}\right) - \exp\left(-\frac{t}{\tau_0}\right)$$

with τ_1 = 0.12 ms (time constant of fast decay), τ_2 = 13 ms (time constant of slow decay), τ_0 = 0.12 ms (time constant of rise phase), ρ = 1.e-5 (proportion of slow phase in decay), and *A* being a normalization constant making the amplitude 60 pA. Parameter values were chosen such that the kinetics of the mEPSC would match events measured in the Calyx of Held (Chang et al., 2015). In Figure 3 traces show three randomly chosen eEPSCs. Representative eEPSC traces shown in Figures 4 and 5 are simulated eEPSCs with the amplitude closest to the mean eEPSC amplitude.

Simulating AP-evoked EPSCs with variable syt

To investigate the effect of variability in the number of syts expressed per SV on variance between simulated AP-evoked traces model (Figure 4), we first had to determine the steady state. For this we computed the probability vector of a single SV to be in the different SV-states at steady state (φ) for n_{syt}=1,…,50. Subsequently, for each SV and each repetition (n=1000) a random number of n_{syt} was

bioRxiv preprint doi: https://doi.org/10.1101/2021.10.22.465434; this version posted October 23, 2021. The copyright holder for this preprint (which was not certified by peer review) is the author/funder, who has granted bioRxiv a license to display the preprint in perpetuity. It is made available under aCC-BY 4.0 International license.

drawn from the Poisson distribution with mean=15. When the value 0 was drawn, it was replaced by n_{syt}=1. Using these values and φ determined for each n_{syt}, we computed the steady state matrix (X(0)) as described above ("Determining the initial state of the system"). To reduce computation time, we evaluated a model containing 100 vesicles 40 times instead of evaluating 4000 vesicles simultaneously. The fusion times obtained when driving the model with the Ca^{2+}-transient were combined afterwards. This is valid since all SVs act independently in the model. For the condition with a variable RRP size, fusion times were selected randomly until the RRP size of that specific repetition was reached. Afterwards, the fusion times were convolved with the mEPSC to obtain simulated AP-evoked responses. To quantify the variance in the traces, we computed the standard deviation of the simulated eEPSCs at each data point (300 data points corresponding to the time interval 0-6ms) and summed those values.

The interpretation of PI(4,5)P_2 concentration

The binding affinities of syt for both Ca^{2+} and PI(4,5)P_2 in the model are based on biochemical experiments performed by van den Bogaart et al. (van den Bogaart *et al.*, 2012). These experiments were carried out in bulk, i.e. the C2AB-domain of syt1 and PI(4,5)P_2 were both dissolved at known concentrations. However, at the release site, PI(4,5)P_2 is not dissolved but is embedded in the inner leaflet of the plasma membrane. Therefore, the estimated, effective PI(4,5)P_2 concentration of 1.11 µM at release sites obtained in this study corresponds to whatever density of PI(4,5)P_2 in the inner leaflet that would lead to the same PI(4,5)P_2-occupancy of SV-anchored syt as its concentration would in bulk. As this density depends on the localization of syt with respect to PI(4,5)P_2 clusters on the plasma membrane, it is currently not possible to recalculate the fitted value of [PI(4,5)P_2] to an actual PI(4,5)P_2 density. However, these considerations have one notable consequence: there are two ways in which the effective PI(4,5)P_2 concentration in the model could be reduced, either by reducing the PI(4,5)P_2 density in the membrane, or by mislocalizing the SV.

Acknowledgements

This work was supported by grants from the Deutsche Forschungsgemeinschaft (Emmy Noether Programme, Project Number 261020751 and the TRR 186, Project Number 278001972 to A.M.W), the Novo Nordisk Foundation (NNF20OC0062958 to S.D.; NNF19OC0058298 to J.B.S and a Young Investigator Award NNF19OC0056047 to A.M.W.), the Lundbeck Foundation (R277-2018-802 to J.B.S.) and the Independent Research Fund Denmark (8020-00228A to J.B.S.). We would like to thank

bioRxiv preprint doi: https://doi.org/10.1101/2021.10.22.465434; this version posted October 23, 2021. The copyright holder for this preprint (which was not certified by peer review) is the author/funder, who has granted bioRxiv a license to display the preprint in perpetuity. It is made available under aCC-BY 4.0 International license.

Ralf Schneggenburger and Holger Taschenberger for providing the experimental Ca^{2+} uncaging dataset and AP-induced Ca^{2+} transient.

Competing Interests

The authors declare no conflicting financial and non-financial interest.

bioRxiv preprint doi: https://doi.org/10.1101/2021.10.22.465434; this version posted October 23, 2021. The copyright holder for this preprint (which was not certified by peer review) is the author/funder, who has granted bioRxiv a license to display the preprint in perpetuity. It is made available under aCC-BY 4.0 International license.

References

Alle, H., Kubota, H., and Geiger, J.R. (2011). Sparse but highly efficient Kv3 outpace BKCa channels in action potential repolarization at hippocampal mossy fiber boutons. J Neurosci *31*, 8001-8012. 10.1523/JNEUROSCI.0972-11.2011.

Araç, D., Chen, X., Khant, H.A., Ubach, J., Ludtke, S.J., Kikkawa, M., Johnson, A.E., Chiu, W., Südhof, T.C., and Rizo, J. (2006). Close membrane-membrane proximity induced by Ca2+-dependent multivalent binding of synaptotagmin-1 to phospholipids. Nature structural & molecular biology *13*, 209-217. 10.1038/nsmb1056.

Arancillo, M., Min, S.W., Gerber, S., Münster-Wandowski, A., Wu, Y.J., Herman, M., Trimbuch, T., Rah, J.C., Ahnert-Hilger, G., Riedel, D., et al. (2013). Titration of Syntaxin1 in mammalian synapses reveals multiple roles in vesicle docking, priming, and release probability. J Neurosci *33*, 16698-16714. 10.1523/jneurosci.0187-13.2013.

Augustin, I., Rosenmund, C., Südhof, T.C., and Brose, N. (1999). Munc13-1 is essential for fusion competence of glutamatergic synaptic vesicles. Nature *400*, 457-461. 10.1038/22768.

Bacaj, T., Wu, D., Burre, J., Malenka, R.C., Liu, X., and Sudhof, T.C. (2015). Synaptotagmin-1 and -7 Are Redundantly Essential for Maintaining the Capacity of the Readily-Releasable Pool of Synaptic Vesicles. PLoS Biol *13*, e1002267. 10.1371/journal.pbio.1002267.

Bacaj, T., Wu, D., Yang, X., Morishita, W., Zhou, P., Xu, W., Malenka, R.C., and Sudhof, T.C. (2013). Synaptotagmin-1 and synaptotagmin-7 trigger synchronous and asynchronous phases of neurotransmitter release. Neuron *80*, 947-959. 10.1016/j.neuron.2013.10.026.

Bai, J., Tucker, W.C., and Chapman, E.R. (2004). PIP2 increases the speed of response of synaptotagmin and steers its membrane-penetration activity toward the plasma membrane. Nature structural & molecular biology *11*, 36-44. 10.1038/nsmb709.

Baker, K., Gordon, S.L., Melland, H., Bumbak, F., Scott, D.J., Jiang, T.J., Owen, D., Turner, B.J., Boyd, S.G., Rossi, M., et al. (2018). SYT1-associated neurodevelopmental disorder: a case series. Brain *141*, 2576-2591. 10.1093/brain/awy209.

Basu, J., Betz, A., Brose, N., and Rosenmund, C. (2007). Munc13-1 C1 domain activation lowers the energy barrier for synaptic vesicle fusion. J Neurosci *27*, 1200-1210. 10.1523/JNEUROSCI.4908-06.2007.

Bohme, M.A., Beis, C., Reddy-Alla, S., Reynolds, E., Mampell, M.M., Grasskamp, A.T., Lutzkendorf, J., Bergeron, D.D., Driller, J.H., Babikir, H., et al. (2016). Active zone scaffolds differentially accumulate Unc13 isoforms to tune Ca(2+) channel-vesicle coupling. Nature neuroscience *19*, 1311-1320. 10.1038/nn.4364.

bioRxiv preprint doi: https://doi.org/10.1101/2021.10.22.465434; this version posted October 23, 2021. The copyright holder for this preprint (which was not certified by peer review) is the author/funder, who has granted bioRxiv a license to display the preprint in perpetuity. It is made available under aCC-BY 4.0 International license.

Bollmann, J.H., Sakmann, B., and Borst, J.G. (2000). Calcium sensitivity of glutamate release in a calyx-type terminal. Science (New York, N.Y.) *289*, 953-957.

Bradberry, M.M., Courtney, N.A., Dominguez, M.J., Lofquist, S.M., Knox, A.T., Sutton, R.B., and Chapman, E.R. (2020). Molecular Basis for Synaptotagmin-1-Associated Neurodevelopmental Disorder. Neuron *107*, 52-64 e57. 10.1016/j.neuron.2020.04.003.

Brewer, K.D., Bacaj, T., Cavalli, A., Camilloni, C., Swarbrick, J.D., Liu, J., Zhou, A., Zhou, P., Barlow, N., Xu, J., et al. (2015). Dynamic binding mode of a Synaptotagmin-1-SNARE complex in solution. Nature structural & molecular biology *22*, 555-564. 10.1038/nsmb.3035.

Burgalossi, A., Jung, S., Meyer, G., Jockusch, W.J., Jahn, O., Taschenberger, H., O'Connor, V.M., Nishiki, T., Takahashi, M., Brose, N., and Rhee, J.S. (2010). SNARE protein recycling by alphaSNAP and betaSNAP supports synaptic vesicle priming. Neuron *68*, 473-487. 10.1016/j.neuron.2010.09.019.

Chang, S., Reim, K., Pedersen, M., Neher, E., Brose, N., and Taschenberger, H. (2015). Complexin stabilizes newly primed synaptic vesicles and prevents their premature fusion at the mouse calyx of held synapse. J Neurosci *35*, 8272-8290. 10.1523/JNEUROSCI.4841-14.2015.

Chang, S., Trimbuch, T., and Rosenmund, C. (2018). Synaptotagmin-1 drives synchronous Ca(2+)-triggered fusion by C2B-domain-mediated synaptic-vesicle-membrane attachment. Nature neuroscience *21*, 33-40. 10.1038/s41593-017-0037-5.

Chen, Y., Wang, Y.H., Zheng, Y., Li, M., Wang, B., Wang, Q.W., Fu, C.L., Liu, Y.N., Li, X., and Yao, J. (2021). Synaptotagmin-1 interacts with PI(4,5)P2 to initiate synaptic vesicle docking in hippocampal neurons. Cell Rep *34*, 108842. 10.1016/j.celrep.2021.108842.

Colquhoun, D., Dowsland, K.A., Beato, M., and Plested, A.J. (2004). How to impose microscopic reversibility in complex reaction mechanisms. Biophysical journal *86*, 3510-3518. 10.1529/biophysj.103.038679.

de Wit, H., Walter, A.M., Milosevic, I., Gulyas-Kovacs, A., Riedel, D., Sorensen, J.B., and Verhage, M. (2009). Synaptotagmin-1 docks secretory vesicles to syntaxin-1/SNAP-25 acceptor complexes. Cell *138*, 935-946. 10.1016/j.cell.2009.07.027.

Fernandez-Chacon, R., Konigstorfer, A., Gerber, S.H., Garcia, J., Matos, M.F., Stevens, C.F., Brose, N., Rizo, J., Rosenmund, C., and Sudhof, T.C. (2001). Synaptotagmin I functions as a calcium regulator of release probability. Nature *410*, 41-49. 10.1038/35065004.

Fernandez, I., Arac, D., Ubach, J., Gerber, S.H., Shin, O., Gao, Y., Anderson, R.G., Sudhof, T.C., and Rizo, J. (2001). Three-dimensional structure of the synaptotagmin 1 C2B-domain: synaptotagmin 1 as a phospholipid binding machine. Neuron *32*, 1057-1069. 10.1016/s0896-6273(01)00548-7.

Geppert, M., Goda, Y., Hammer, R.E., Li, C., Rosahl, T.W., Stevens, C.F., and Sudhof, T.C. (1994). Synaptotagmin I: a major Ca2+ sensor for transmitter release at a central synapse. Cell *79*, 717-727.

bioRxiv preprint doi: https://doi.org/10.1101/2021.10.22.465434; this version posted October 23, 2021. The copyright holder for this preprint (which was not certified by peer review) is the author/funder, who has granted bioRxiv a license to display the preprint in perpetuity. It is made available under aCC-BY 4.0 International license.

Gillespie, D.T. (2007). Stochastic Simulation of Chemical Kinetics. Annual Review of Physical Chemistry *58*, 35-55. 10.1146/annurev.physchem.58.032806.104637.

Gruget, C., Bello, O., Coleman, J., Krishnakumar, S.S., Perez, E., Rothman, J.E., Pincet, F., and Donaldson, S.H., Jr. (2020). Synaptotagmin-1 membrane binding is driven by the C2B domain and assisted cooperatively by the C2A domain. Sci Rep *10*, 18011. 10.1038/s41598-020-74923-y.

Harper, C.B., Small, C., Davenport, E.C., Low, D.W., Smillie, K.J., Martínez-Mármol, R., Meunier, F.A., and Cousin, M.A. (2020). An Epilepsy-Associated SV2A Mutation Disrupts Synaptotagmin-1 Expression and Activity-Dependent Trafficking. The Journal of Neuroscience *40*, 4586-4595. 10.1523/jneurosci.0210-20.2020.

Heidelberger, R., Heinemann, C., Neher, E., and Matthews, G. (1994). Calcium dependence of the rate of exocytosis in a synaptic terminal. Nature *371*, 513-515. 10.1038/371513a0.

Helmchen, F., Borst, J.G., and Sakmann, B. (1997). Calcium dynamics associated with a single action potential in a CNS presynaptic terminal. Biophysical journal *72*, 1458-1471. 10.1016/s0006-3495(97)78792-7.

Honigmann, A., van den Bogaart, G., Iraheta, E., Risselada, H.J., Milovanovic, D., Mueller, V., Mullar, S., Diederichsen, U., Fasshauer, D., Grubmuller, H., et al. (2013). Phosphatidylinositol 4,5-bisphosphate clusters act as molecular beacons for vesicle recruitment. Nature structural & molecular biology *20*, 679-686. 10.1038/nsmb.2570.

Hui, E., Gaffaney, J.D., Wang, Z., Johnson, C.P., Evans, C.S., and Chapman, E.R. (2011). Mechanism and function of synaptotagmin-mediated membrane apposition. Nature structural & molecular biology *18*, 813-821. 10.1038/nsmb.2075.

Imig, C., Min, S.W., Krinner, S., Arancillo, M., Rosenmund, C., Sudhof, T.C., Rhee, J., Brose, N., and Cooper, B.H. (2014). The morphological and molecular nature of synaptic vesicle priming at presynaptic active zones. Neuron *84*, 416-431. 10.1016/j.neuron.2014.10.009.

Jahn, R., and Fasshauer, D. (2012). Molecular machines governing exocytosis of synaptic vesicles. Nature *490*, 201-207. 10.1038/nature11320.

Kaempf, N., Kochlamazashvili, G., Puchkov, D., Maritzen, T., Bajjalieh, S.M., Kononenko, N.L., and Haucke, V. (2015). Overlapping functions of stonin 2 and SV2 in sorting of the calcium sensor synaptotagmin 1 to synaptic vesicles. Proceedings of the National Academy of Sciences of the United States of America *112*, 7297-7302. 10.1073/pnas.1501627112.

Kaeser, P.S., and Regehr, W.G. (2017). The readily releasable pool of synaptic vesicles. Curr Opin Neurobiol *43*, 63-70. 10.1016/j.conb.2016.12.012.

Kobbersmed, J.R., Grasskamp, A.T., Jusyte, M., Bohme, M.A., Ditlevsen, S., Sorensen, J.B., and Walter, A.M. (2020). Rapid regulation of vesicle priming explains synaptic facilitation despite heterogeneous vesicle:Ca(2+) channel distances. Elife *9*. 10.7554/eLife.51032.

bioRxiv preprint doi: https://doi.org/10.1101/2021.10.22.465434; this version posted October 23, 2021. The copyright holder for this preprint (which was not certified by peer review) is the author/funder, who has granted bioRxiv a license to display the preprint in perpetuity. It is made available under aCC-BY 4.0 International license.

Kochubey, O., Babai, N., and Schneggenburger, R. (2016). A Synaptotagmin Isoform Switch during the Development of an Identified CNS Synapse. Neuron *91*, 1183. 10.1016/j.neuron.2016.08.024.

Kochubey, O., and Schneggenburger, R. (2011). Synaptotagmin Increases the Dynamic Range of Synapses by Driving Ca2+-Evoked Release and by Clamping a Near-Linear Remaining Ca2+ Sensor. Neuron *69*, 736-748. 10.1016/j.neuron.2011.01.013.

Lai, A.L., Tamm, L.K., Ellena, J.F., and Cafiso, D.S. (2011). Synaptotagmin 1 modulates lipid acyl chain order in lipid bilayers by demixing phosphatidylserine. The Journal of biological chemistry *286*, 25291-25300. 10.1074/jbc.M111.258848.

Lee, J., Guan, Z., Akbergenova, Y., and Littleton, J.T. (2013). Genetic analysis of synaptotagmin C2 domain specificity in regulating spontaneous and evoked neurotransmitter release. J Neurosci *33*, 187-200. 10.1523/JNEUROSCI.3214-12.2013.

Li, L., Shin, O.H., Rhee, J.S., Arac, D., Rah, J.C., Rizo, J., Sudhof, T., and Rosenmund, C. (2006). Phosphatidylinositol phosphates as co-activators of Ca2+ binding to C2 domains of synaptotagmin 1. The Journal of biological chemistry *281*, 15845-15852. 10.1074/jbc.M600888200.

Lin, C.C., Seikowski, J., Perez-Lara, A., Jahn, R., Hobartner, C., and Walla, P.J. (2014). Control of membrane gaps by synaptotagmin-Ca2+ measured with a novel membrane distance ruler. Nat Commun *5*, 5859. 10.1038/ncomms6859.

Littleton, J.T., Stern, M., Schulze, K., Perin, M., and Bellen, H.J. (1993). Mutational analysis of Drosophila synaptotagmin demonstrates its essential role in Ca(2+)-activated neurotransmitter release. Cell *74*, 1125-1134. 10.1016/0092-8674(93)90733-7.

Liu, H., Bai, H., Hui, E., Yang, L., Evans, C.S., Wang, Z., Kwon, S.E., and Chapman, E.R. (2014). Synaptotagmin 7 functions as a Ca2+-sensor for synaptic vesicle replenishment. Elife *3*, e01524. 10.7554/eLife.01524.

Liu, X., Seven, A.B., Camacho, M., Esser, V., Xu, J., Trimbuch, T., Quade, B., Su, L., Ma, C., Rosenmund, C., and Rizo, J. (2016). Functional synergy between the Munc13 C-terminal C1 and C2 domains. Elife *5*. 10.7554/eLife.13696.

Lou, X., Scheuss, V., and Schneggenburger, R. (2005). Allosteric modulation of the presynaptic Ca2+ sensor for vesicle fusion. Nature *435*, 497-501. 10.1038/nature03568.

Luo, F., and Sudhof, T.C. (2017). Synaptotagmin-7-Mediated Asynchronous Release Boosts High-Fidelity Synchronous Transmission at a Central Synapse. Neuron *94*, 826-839 e823. 10.1016/j.neuron.2017.04.020.

Mackler, J.M., Drummond, J.A., Loewen, C.A., Robinson, I.M., and Reist, N.E. (2002). The C(2)B Ca(2+)-binding motif of synaptotagmin is required for synaptic transmission in vivo. Nature *418*, 340-344. 10.1038/nature00846.

bioRxiv preprint doi: https://doi.org/10.1101/2021.10.22.465434; this version posted October 23, 2021. The copyright holder for this preprint (which was not certified by peer review) is the author/funder, who has granted bioRxiv a license to display the preprint in perpetuity. It is made available under aCC-BY 4.0 International license.

Martens, S., Kozlov, M.M., and McMahon, H.T. (2007). How synaptotagmin promotes membrane fusion. Science (New York, N.Y.) *316*, 1205-1208. 10.1126/science.1142614.

Maximov, A., Lao, Y., Li, H., Chen, X., Rizo, J., Sorensen, J.B., and Sudhof, T.C. (2008). Genetic analysis of synaptotagmin-7 function in synaptic vesicle exocytosis. Proceedings of the National Academy of Sciences of the United States of America *105*, 3986-3991. 10.1073/pnas.0712372105.

Milosevic, I., Sorensen, J.B., Lang, T., Krauss, M., Nagy, G., Haucke, V., Jahn, R., and Neher, E. (2005). Plasmalemmal phosphatidylinositol-4,5-bisphosphate level regulates the releasable vesicle pool size in chromaffin cells. J Neurosci *25*, 2557-2565. 10.1523/JNEUROSCI.3761-04.2005.

Mohrmann, R., de Wit, H., Connell, E., Pinheiro, P.S., Leese, C., Bruns, D., Davletov, B., Verhage, M., and Sorensen, J.B. (2013). Synaptotagmin interaction with SNAP-25 governs vesicle docking, priming, and fusion triggering. J Neurosci *33*, 14417-14430. 10.1523/JNEUROSCI.1236-13.2013.

Mohrmann, R., de Wit, H., Verhage, M., Neher, E., and Sørensen, J.B. (2010). Fast vesicle fusion in living cells requires at least three SNARE complexes. Science (New York, N.Y.) *330*, 502-505. 10.1126/science.1193134.

Mutch, S.A., Kensel-Hammes, P., Gadd, J.C., Fujimoto, B.S., Allen, R.W., Schiro, P.G., Lorenz, R.M., Kuyper, C.L., Kuo, J.S., Bajjalieh, S.M., and Chiu, D.T. (2011). Protein quantification at the single vesicle level reveals that a subset of synaptic vesicle proteins are trafficked with high precision. J Neurosci *31*, 1461-1470. 10.1523/JNEUROSCI.3805-10.2011.

Neher, E., and Brose, N. (2018). Dynamically Primed Synaptic Vesicle States: Key to Understand Synaptic Short-Term Plasticity. Neuron *100*, 1283-1291. 10.1016/j.neuron.2018.11.024.

Neher, E., and Sakaba, T. (2001). Combining deconvolution and noise analysis for the estimation of transmitter release rates at the calyx of held. J Neurosci *21*, 444-461. 10.1523/jneurosci.21-02-00444.2001.

Nishiki, T., and Augustine, G.J. (2004). Dual roles of the C2B domain of synaptotagmin I in synchronizing Ca2+-dependent neurotransmitter release. J Neurosci *24*, 8542-8550. 10.1523/JNEUROSCI.2545-04.2004.

Nyenhuis, S.B., Karandikar, N., Kiessling, V., Kreutzberger, A.J.B., Thapa, A., Liang, B., Tamm, L.K., and Cafiso, D.S. (2021). Conserved arginine residues in synaptotagmin 1 regulate fusion pore expansion through membrane contact. Nat Commun *12*, 761. 10.1038/s41467-021-21090-x.

Nyenhuis, S.B., Thapa, A., and Cafiso, D.S. (2019). Phosphatidylinositol 4,5 Bisphosphate Controls the cis and trans Interactions of Synaptotagmin 1. Biophysical journal *117*, 247-257. 10.1016/j.bpj.2019.06.016.

Perez-Lara, A., Thapa, A., Nyenhuis, S.B., Nyenhuis, D.A., Halder, P., Tietzel, M., Tittmann, K., Cafiso, D.S., and Jahn, R. (2016). PtdInsP2 and PtdSer cooperate to trap synaptotagmin-1 to the plasma membrane in the presence of calcium. Elife *5*. 10.7554/eLife.15886.

bioRxiv preprint doi: https://doi.org/10.1101/2021.10.22.465434; this version posted October 23, 2021. The copyright holder for this preprint (which was not certified by peer review) is the author/funder, who has granted bioRxiv a license to display the preprint in perpetuity. It is made available under aCC-BY 4.0 International license.

Quade, B., Camacho, M., Zhao, X., Orlando, M., Trimbuch, T., Xu, J., Li, W., Nicastro, D., Rosenmund, C., and Rizo, J. (2019). Membrane bridging by Munc13-1 is crucial for neurotransmitter release. Elife *8*. 10.7554/eLife.42806.

Radhakrishnan, A., Li, X., Grushin, K., Krishnakumar, S.S., Liu, J., and Rothman, J.E. (2021). Symmetrical arrangement of proteins under release-ready vesicles in presynaptic terminals. Proceedings of the National Academy of Sciences of the United States of America *118*. 10.1073/pnas.2024029118.

Radhakrishnan, A., Stein, A., Jahn, R., and Fasshauer, D. (2009). The Ca2+ affinity of synaptotagmin 1 is markedly increased by a specific interaction of its C2B domain with phosphatidylinositol 4,5-bisphosphate. The Journal of biological chemistry *284*, 25749-25760. 10.1074/jbc.M109.042499.

Rothman, J.E., Krishnakumar, S.S., Grushin, K., and Pincet, F. (2017). Hypothesis - buttressed rings assemble, clamp, and release SNAREpins for synaptic transmission. FEBS Lett *591*, 3459-3480. 10.1002/1873-3468.12874.

Ruiter, M., Kádková, A., Scheutzow, A., Malsam, J., Söllner, T.H., and Sørensen, J.B. (2019). An Electrostatic Energy Barrier for SNARE-Dependent Spontaneous and Evoked Synaptic Transmission. Cell Rep *26*, 2340-2352.e2345. 10.1016/j.celrep.2019.01.103.

Schneggenburger, R., and Neher, E. (2000). Intracellular calcium dependence of transmitter release rates at a fast central synapse. Nature *406*, 889-893. 10.1038/35022702.

Schotten, S., Meijer, M., Walter, A.M., Huson, V., Mamer, L., Kalogreades, L., ter Veer, M., Ruiter, M., Brose, N., Rosenmund, C., et al. (2015). Additive effects on the energy barrier for synaptic vesicle fusion cause supralinear effects on the vesicle fusion rate. Elife *4*, e05531. 10.7554/eLife.05531.

Schupp, M., Malsam, J., Ruiter, M., Scheutzow, A., Wierda, K.D., Sollner, T.H., and Sorensen, J.B. (2016). Interactions Between SNAP-25 and Synaptotagmin-1 Are Involved in Vesicle Priming, Clamping Spontaneous and Stimulating Evoked Neurotransmission. J Neurosci *36*, 11865-11880. 10.1523/JNEUROSCI.1011-16.2016.

Seven, A.B., Brewer, K.D., Shi, L., Jiang, Q.X., and Rizo, J. (2013). Prevalent mechanism of membrane bridging by synaptotagmin-1. Proceedings of the National Academy of Sciences of the United States of America *110*, E3243-3252. 10.1073/pnas.1310327110.

Shi, L., Shen, Q.T., Kiel, A., Wang, J., Wang, H.W., Melia, T.J., Rothman, J.E., and Pincet, F. (2012). SNARE proteins: one to fuse and three to keep the nascent fusion pore open. Science (New York, N.Y.) *335*, 1355-1359. 10.1126/science.1214984.

Silva, M., Tran, V., and Marty, A. (2021). Calcium-dependent docking of synaptic vesicles. Trends Neurosci. 10.1016/j.tins.2021.04.003.

bioRxiv preprint doi: https://doi.org/10.1101/2021.10.22.465434; this version posted October 23, 2021. The copyright holder for this preprint (which was not certified by peer review) is the author/funder, who has granted bioRxiv a license to display the preprint in perpetuity. It is made available under aCC-BY 4.0 International license.

Sinha, R., Ahmed, S., Jahn, R., and Klingauf, J. (2011). Two synaptobrevin molecules are sufficient for vesicle fusion in central nervous system synapses. Proceedings of the National Academy of Sciences of the United States of America *108*, 14318-14323. 10.1073/pnas.1101818108.

Sudhof, T.C. (2002). Synaptotagmins: why so many? The Journal of biological chemistry *277*, 7629-7632. 10.1074/jbc.R100052200.

Sudhof, T.C. (2013). Neurotransmitter release: the last millisecond in the life of a synaptic vesicle. Neuron *80*, 675-690. 10.1016/j.neuron.2013.10.022.

Sun, J., Pang, Z.P., Qin, D., Fahim, A.T., Adachi, R., and Sudhof, T.C. (2007). A dual-Ca2+-sensor model for neurotransmitter release in a central synapse. Nature *450*, 676-682. 10.1038/nature06308.

Takamori, S., Holt, M., Stenius, K., Lemke, E.A., Grønborg, M., Riedel, D., Urlaub, H., Schenck, S., Brügger, B., Ringler, P., et al. (2006). Molecular anatomy of a trafficking organelle. Cell *127*, 831-846. 10.1016/j.cell.2006.10.030.

Tawfik, B., Martins, J.S., Houy, S., Imig, C., Pinheiro, P.S., Wojcik, S.M., Brose, N., Cooper, B.H., and Sørensen, J.B. (2021). Synaptotagmin-7 places dense-core vesicles at the cell membrane to promote Munc13-2- and Ca(2+)-dependent priming. Elife *10*. 10.7554/eLife.64527.

van den Bogaart, G., Meyenberg, K., Diederichsen, U., and Jahn, R. (2012). Phosphatidylinositol 4,5-bisphosphate increases Ca2+ affinity of synaptotagmin-1 by 40-fold. The Journal of biological chemistry *287*, 16447-16453. 10.1074/jbc.M112.343418.

van den Bogaart, G., Meyenberg, K., Risselada, H.J., Amin, H., Willig, K.I., Hubrich, B.E., Dier, M., Hell, S.W., Grubmuller, H., Diederichsen, U., and Jahn, R. (2011a). Membrane protein sequestering by ionic protein-lipid interactions. Nature *479*, 552-555. 10.1038/nature10545.

van den Bogaart, G., Thutupalli, S., Risselada, J.H., Meyenberg, K., Holt, M., Riedel, D., Diederichsen, U., Herminghaus, S., Grubmuller, H., and Jahn, R. (2011b). Synaptotagmin-1 may be a distance regulator acting upstream of SNARE nucleation. Nature structural & molecular biology *18*, 805-812. 10.1038/nsmb.2061.

Varoqueaux, F., Sigler, A., Rhee, J.S., Brose, N., Enk, C., Reim, K., and Rosenmund, C. (2002). Total arrest of spontaneous and evoked synaptic transmission but normal synaptogenesis in the absence of Munc13-mediated vesicle priming. Proceedings of the National Academy of Sciences of the United States of America *99*, 9037-9042. 10.1073/pnas.122623799.

Verhage, M., and Sorensen, J.B. (2020). SNAREopathies: Diversity in Mechanisms and Symptoms. Neuron *107*, 22-37. 10.1016/j.neuron.2020.05.036.

Verhage, M., and Sørensen, J.B. (2008). Vesicle docking in regulated exocytosis. Traffic (Copenhagen, Denmark) *9*, 1414-1424. 10.1111/j.1600-0854.2008.00759.x.

bioRxiv preprint doi: https://doi.org/10.1101/2021.10.22.465434; this version posted October 23, 2021. The copyright holder for this preprint (which was not certified by peer review) is the author/funder, who has granted bioRxiv a license to display the preprint in perpetuity. It is made available under aCC-BY 4.0 International license.

Vevea, J.D., Kusick, G.F., Courtney, K.C., Chen, E., Watanabe, S., and Chapman, E.R. (2021). Synaptotagmin 7 is targeted to the axonal plasma membrane through gamma-secretase processing to promote synaptic vesicle docking in mouse hippocampal neurons. Elife *10*. 10.7554/eLife.67261.

Voleti, R., Tomchick, D.R., Sudhof, T.C., and Rizo, J. (2017). Exceptionally tight membrane-binding may explain the key role of the synaptotagmin-7 C2A domain in asynchronous neurotransmitter release. Proceedings of the National Academy of Sciences of the United States of America *114*, E8518-E8527. 10.1073/pnas.1710708114.

Walter, A.M., Wiederhold, K., Bruns, D., Fasshauer, D., and Sørensen, J.B. (2010). Synaptobrevin N-terminally bound to syntaxin-SNAP-25 defines the primed vesicle state in regulated exocytosis. The Journal of cell biology *188*, 401-413. 10.1083/jcb.200907018.

Wang, L.Y., Neher, E., and Taschenberger, H. (2008). Synaptic vesicles in mature calyx of Held synapses sense higher nanodomain calcium concentrations during action potential-evoked glutamate release. J Neurosci *28*, 14450-14458. 10.1523/JNEUROSCI.4245-08.2008.

Weber, J.P., Reim, K., and Sørensen, J.B. (2010). Opposing functions of two sub-domains of the SNARE-complex in neurotransmission. The EMBO journal *29*, 2477-2490. 10.1038/emboj.2010.130.

Wen, H., Linhoff, M.W., McGinley, M.J., Li, G.L., Corson, G.M., Mandel, G., and Brehm, P. (2010). Distinct roles for two synaptotagmin isoforms in synchronous and asynchronous transmitter release at zebrafish neuromuscular junction. Proceedings of the National Academy of Sciences of the United States of America *107*, 13906-13911. 10.1073/pnas.1008598107.

Wolfel, M., Lou, X., and Schneggenburger, R. (2007). A mechanism intrinsic to the vesicle fusion machinery determines fast and slow transmitter release at a large CNS synapse. J Neurosci *27*, 3198-3210. 10.1523/JNEUROSCI.4471-06.2007.

Wölfel, M., and Schneggenburger, R. (2003). Presynaptic capacitance measurements and Ca2+ uncaging reveal submillisecond exocytosis kinetics and characterize the Ca2+ sensitivity of vesicle pool depletion at a fast CNS synapse. J Neurosci *23*, 7059-7068. 10.1523/jneurosci.23-18-07059.2003.

Xu, J., Camacho, M., Xu, Y., Esser, V., Liu, X., Trimbuch, T., Pan, Y.Z., Ma, C., Tomchick, D.R., Rosenmund, C., and Rizo, J. (2017). Mechanistic insights into neurotransmitter release and presynaptic plasticity from the crystal structure of Munc13-1 C1C2BMUN. Elife *6*. 10.7554/eLife.22567.

Xu, J., Mashimo, T., and Sudhof, T.C. (2007). Synaptotagmin-1, -2, and -9: Ca(2+) sensors for fast release that specify distinct presynaptic properties in subsets of neurons. Neuron *54*, 567-581. 10.1016/j.neuron.2007.05.004.

bioRxiv preprint doi: https://doi.org/10.1101/2021.10.22.465434; this version posted October 23, 2021. The copyright holder for this preprint (which was not certified by peer review) is the author/funder, who has granted bioRxiv a license to display the preprint in perpetuity. It is made available under aCC-BY 4.0 International license.

Xue, M., Ma, C., Craig, T.K., Rosenmund, C., and Rizo, J. (2008). The Janus-faced nature of the C(2)B domain is fundamental for synaptotagmin-1 function. Nature structural & molecular biology *15*, 1160-1168. 10.1038/nsmb.1508.

Yao, J., Gaffaney, J.D., Kwon, S.E., and Chapman, E.R. (2011). Doc2 is a Ca2+ sensor required for asynchronous neurotransmitter release. Cell *147*, 666-677. 10.1016/j.cell.2011.09.046.

Zhou, Q., Lai, Y., Bacaj, T., Zhao, M., Lyubimov, A.Y., Uervirojnangkoorn, M., Zeldin, O.B., Brewster, A.S., Sauter, N.K., Cohen, A.E., et al. (2015). Architecture of the synaptotagmin-SNARE machinery for neuronal exocytosis. Nature *525*, 62-67. 10.1038/nature14975.

Zhou, Q., Zhou, P., Wang, A.L., Wu, D., Zhao, M., Sudhof, T.C., and Brunger, A.T. (2017). The primed SNARE-complexin-synaptotagmin complex for neuronal exocytosis. Nature *548*, 420-425. 10.1038/nature23484.

bioRxiv preprint doi: https://doi.org/10.1101/2021.10.22.465434; this version posted October 23, 2021. The copyright holder for this preprint (which was not certified by peer review) is the author/funder, who has granted bioRxiv a license to display the preprint in perpetuity. It is made available under aCC-BY 4.0 International license.

Supplementary figures

Figure 1 – Figure supplement 1

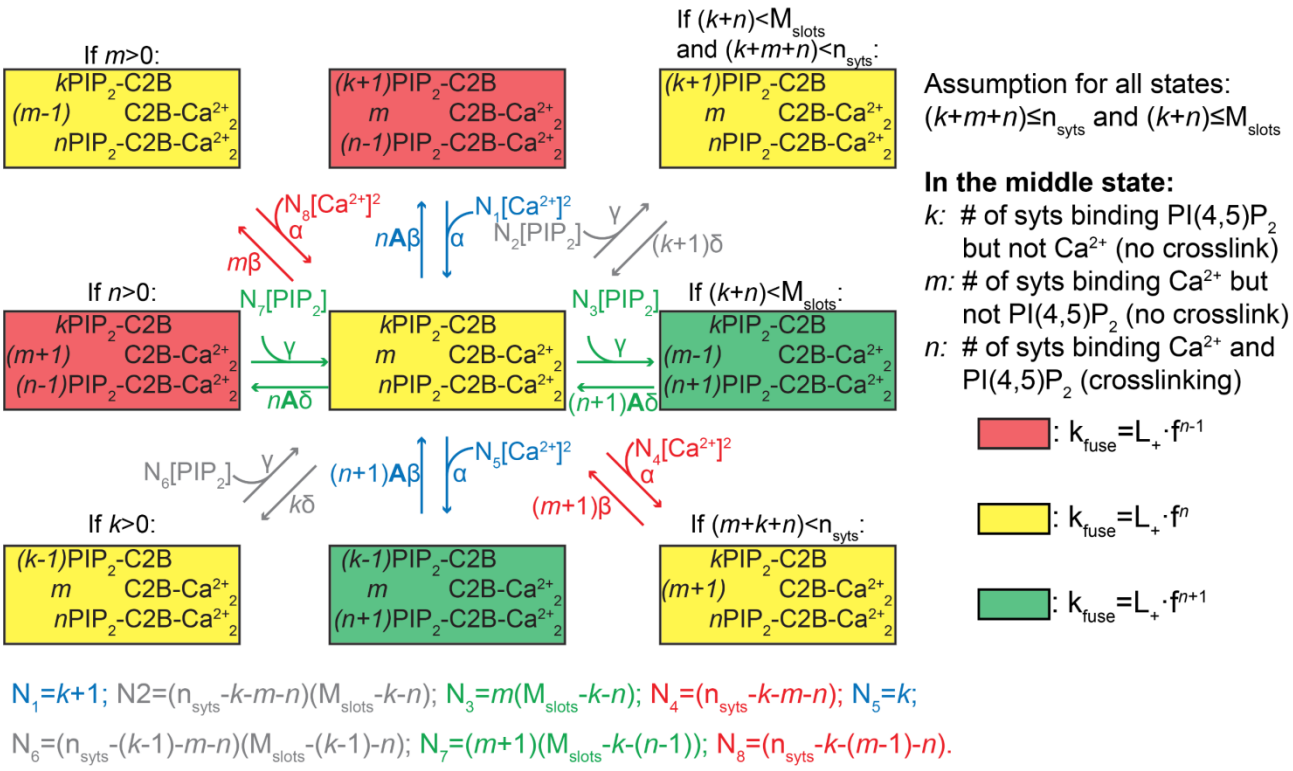

Figure 1 – figure supplement 1: Reaction scheme for all syt reactions of an entire SV. The diagram shows the possible (un)binding reactions and indicates the relative fusion rate of an SV with n_{syts} syts and M_{slots} slots. The state in the center of the diagram represents an SV with k syts having bound only PI(4,5)P_2, m syts having bound only two Ca^{2+}, and n syts having formed crosslinks by binding both PI(4,5)P_2 and two Ca^{2+}. From this state, the SV can (un)bind Ca^{2+} or PI(4,5)P_2 (unbinding moves the SV to the state to the left or up, binding to the right or down). The number of syts, n_{syts}, and the number of slots, M_{slots}, limit the possible number of syts engaging in ligand binding in general and in binding of PI(4,5)P_2, respectively, which is indicated by the assumption in the top right corner. Whether the SV can undergo a specific reaction (that is, whether a certain state exists and the SV can transit to it) depends on its current binding state as indicated by the assumptions above some of the states. The color shading of the states indicates the value of the fusion rate relative to the other states in the diagram. Yellow shading means a fusion rate equal to that from the state in the center. Red and green shading means a factor f lower and higher fusion rate, respectively. For detailed description of the reaction rate equations, see Methods.

bioRxiv preprint doi: https://doi.org/10.1101/2021.10.22.465434; this version posted October 23, 2021. The copyright holder for this preprint (which was not certified by peer review) is the author/funder, who has granted bioRxiv a license to display the preprint in perpetuity. It is made available under aCC-BY 4.0 International license.

Figure 1 – Figure supplement 2

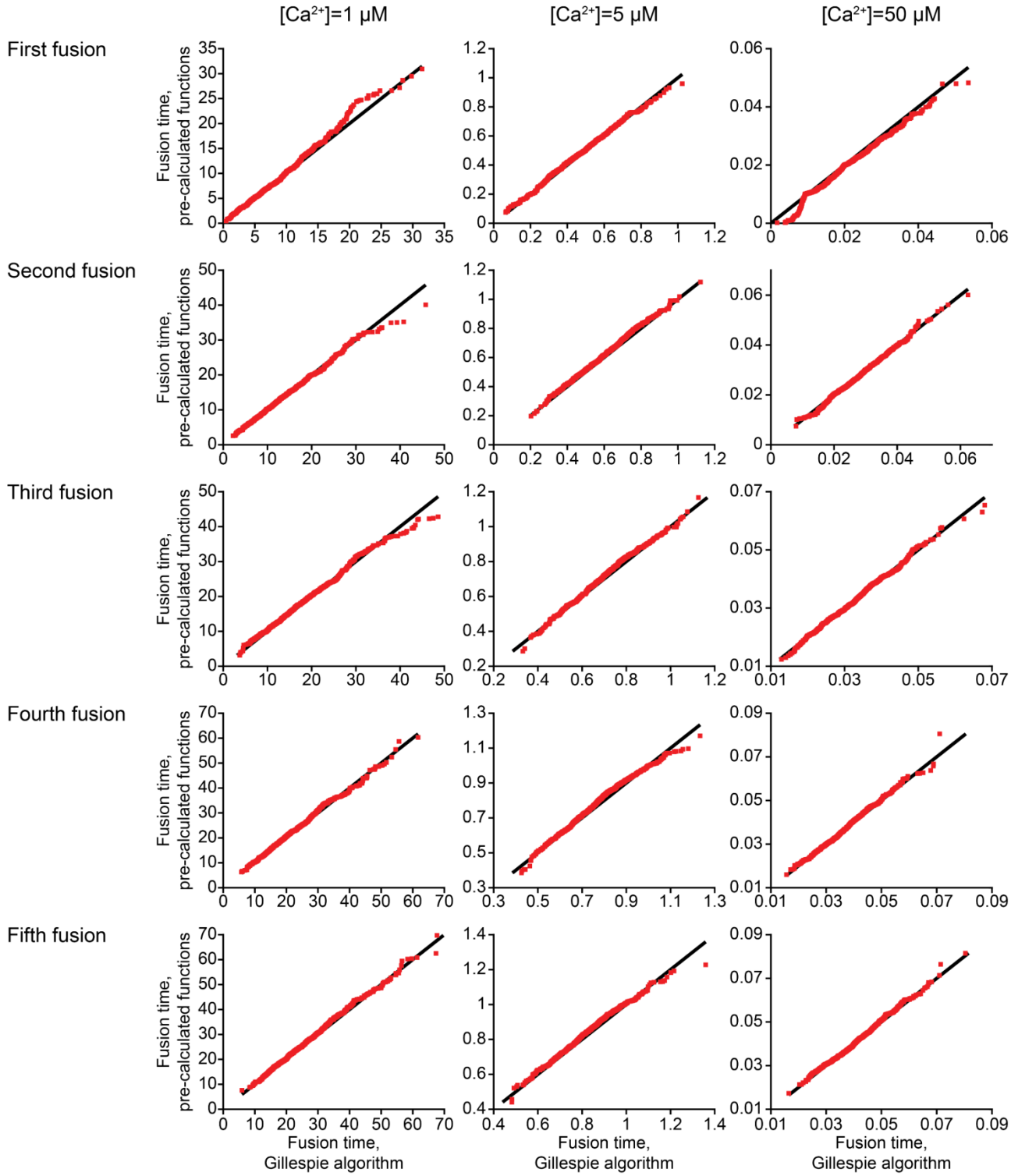

Figure 1 – Figure supplement 2: Comparing the two different model implementations. QQ-plots comparing the first five fusion times obtained using stochastic simulations with an implementation based on the analytical solution of the model (pre-calculated functions) and using the Gillespie algorithm for three different $[Ca^{2+}]_i$. Black line respresent 1:1 correspondence. Red squares indicate fusion time simulated with both methods for 1000 repetitions.

bioRxiv preprint doi: https://doi.org/10.1101/2021.10.22.465434; this version posted October 23, 2021. The copyright holder for this preprint (which was not certified by peer review) is the author/funder, who has granted bioRxiv a license to display the preprint in perpetuity. It is made available under aCC-BY 4.0 International license.

Figure 2 – figure supplement 1

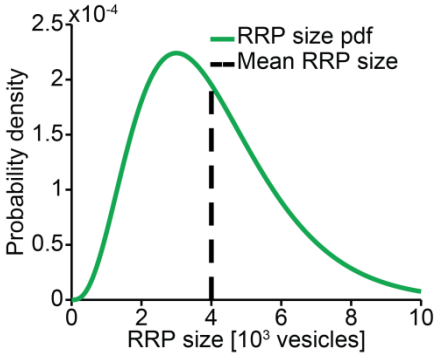

Figure 2 – figure supplement 1: RRP distribution. We assumed the RRP size to follow a gamma distribution with mean 4000 and SD 2000.

bioRxiv preprint doi: https://doi.org/10.1101/2021.10.22.465434; this version posted October 23, 2021. The copyright holder for this preprint (which was not certified by peer review) is the author/funder, who has granted bioRxiv a license to display the preprint in perpetuity. It is made available under aCC-BY 4.0 International license.

Figure 2 – figure supplement 2

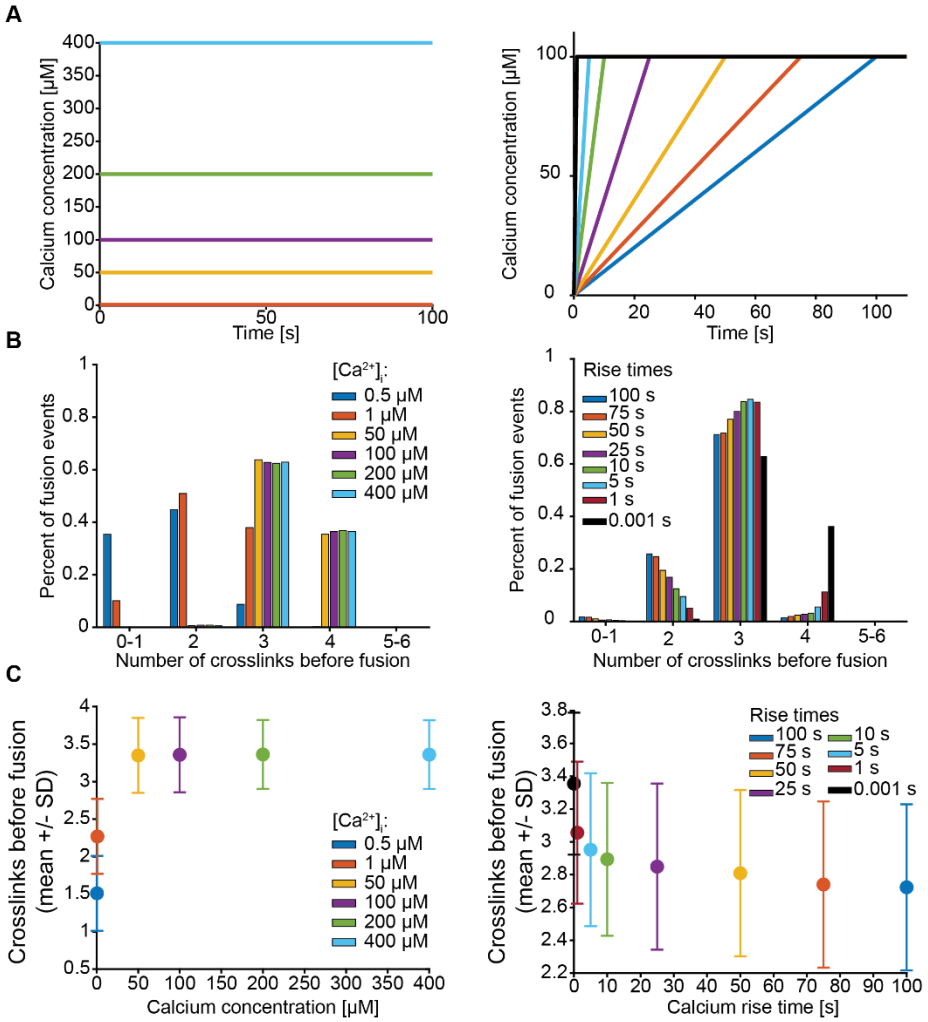

Figure 2 – figure supplement 2: Exploration of the number of crosslinks formed before fusion of an SV with M_{slots}=6A). The Ca^{2+} signal used in simulations with step (left) and ramp (right) Ca^{2+} functions. In simulations with step Ca^{2+} the concentrations rises instantly at t=0 from the basal Ca^{2+} of 50 nM to various constant concentrations. In simulations with ramp Ca^{2+} the Ca^{2+} concentration increases linearly from the basal concentration of 50 nM to 100 µM Ca^{2+} with various rise times. **B)** The number of crosslinks formed before fusion for various Ca^{2+} concentrations (step Ca^{2+}, left) or Ca^{2+} rise times (ramp Ca^{2+}, right) as depicted in A. The bars show percentages of 10000 stochastically simulated SVs. The number of crosslinks formed before fusion increases with increasing step Ca^{2+} concentrations and decreasing Ca^{2+} rise times. At high concentrations or fast rise times, most fusions take place after forming 3-4 crosslinks. **C)** Average number of crosslinks formed before fusion in simulations of 10000 SVs with Ca^{2+} signals as depicted in A. The average number of crosslinks formed before fusion increases with step Ca^{2+} concentration and decreases with increasing Ca^{2+} rise time. A plateau is reached at an average of 3.4 crosslinks at high step Ca^{2+} concentrations. Error bars show ± standard deviation.

bioRxiv preprint doi: https://doi.org/10.1101/2021.10.22.465434; this version posted October 23, 2021. The copyright holder for this preprint (which was not certified by peer review) is the author/funder, who has granted bioRxiv a license to display the preprint in perpetuity. It is made available under aCC-BY 4.0 International license.

Figure 2 – figure supplement 3

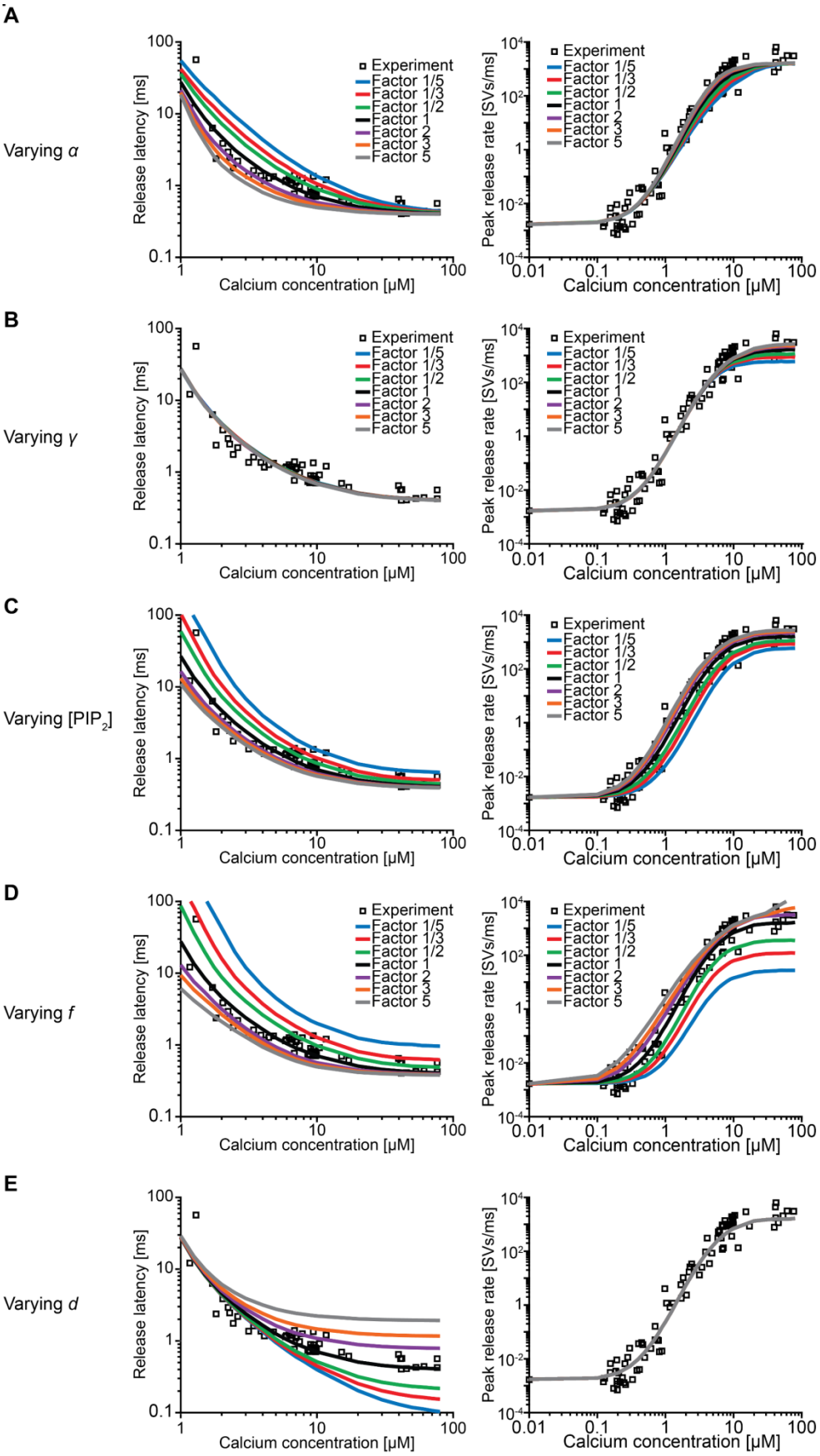

Figure 2 – figure supplement 3: Effect of the free parameters on release latencies and peak release rates.

bioRxiv preprint doi: https://doi.org/10.1101/2021.10.22.465434; this version posted October 23, 2021. The copyright holder for this preprint (which was not certified by peer review) is the author/funder, who has granted bioRxiv a license to display the preprint in perpetuity. It is made available under aCC-BY 4.0 International license.

A-E) Effect on release latencies (left) and peak release rates (right) when varying *α* (A), *γ* (B), [PI(4,5)P_2] (C), *f* (D), and *d* (E). The best-fit values of each of the parameters were increased and decreased by a factor 2, 3 and 5. Varying α and γ leads to a change in β and δ so that the measured affinities for both Ca^{2+} and PI(4,5)P_2 are still matched (van den Bogaart *et al.*, 2012). (**A)** When varying *α* the release latency is mostly affected in the middle range of $[Ca^{2+}]_i$. The effect on the peak release rates is very small **B)** The effect of varying *γ* on release latency is a bit larger compared to varying α(A), but still modest. The effect of varying γ on peak release is larger at high $[Ca^{2+}]_i$ compared to low $[Ca^{2+}]_i$ reflecting that at high $[Ca^{2+}]_i$ PI(4,5)P_2 binding limits crosslink formation. **C)** Varying [PI(4,5)P_2] has a large effect on the release latencies and peak release rates. The effect of varying [PI(4,5)P_2] is much larger compared to varying γ, as changing [PI(4,5)P2] only affects the binding rate of PI(4,5)P_2, whereas changing γ leads to an equal change in δ to match the published affinity values. Furthermore [PI(4,5)P_2] affects the steady state distribution. **D)** Varying *f* has a large effect on both release latency and fusion rate, as it directly impacts the effect of crosslink formation on SV fusion rates. **E)** Varying the added delay, *d*, only shifts the release latencies linearly and does not affect the peak release rates. Experimental data points in these figures are replotted from Kochubey and Schneggenburger (Kochubey and Schneggenburger, 2011).

bioRxiv preprint doi: https://doi.org/10.1101/2021.10.22.465434; this version posted October 23, 2021. The copyright holder for this preprint (which was not certified by peer review) is the author/funder, who has granted bioRxiv a license to display the preprint in perpetuity. It is made available under aCC-BY 4.0 International license.

Figure 3 – figure supplement 1

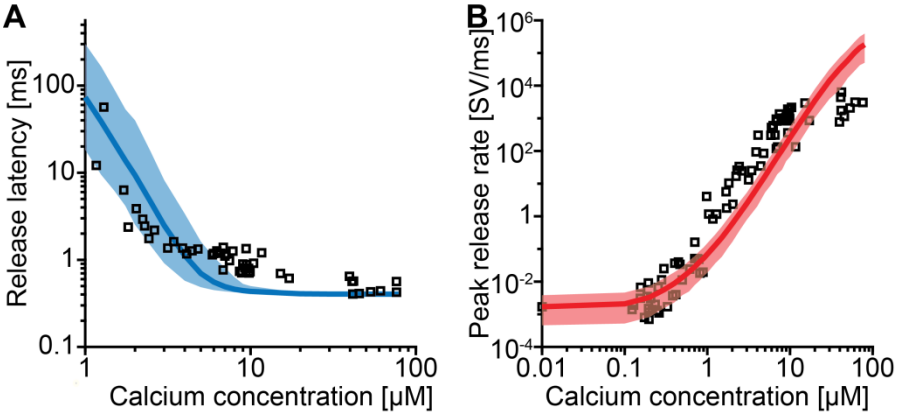

Figure 3 – figure supplement 1: Fitting of the model without allosteric interaction between Ca^{2+} and $PI(4,5)P_2$ fails to reproduce the Ca^{2+}-dependency of NT release. A-B) The best fit results for a model with 3 slots and no allosteric interaction between Ca^{2+} and $PI(4,5)P_2$ (A=1). In A the median release latency and the 95% prediction interval of the best fit model are shown. Note that the y-axis range is different from Figure3A, but the proportions figure scaling is maintained to help comparison. B) The mean maximal fusion rate as a function of $[Ca^{2+}]_i$ and the corresponding 95% prediction interval. Best fit parameters used to generate these curves are: α=2.174 $\mu M^{-2}s^{-1}$, γ=6.773e^5 $\mu M^{-1}s^{-1}$, $[PI(4,5)P_2]$=2991 μM, f=3.943e^5, d=0.4036 ms. Experimental data points in the figures are replotted from Kochubey and Schneggenburger (2011).

bioRxiv preprint doi: https://doi.org/10.1101/2021.10.22.465434; this version posted October 23, 2021. The copyright holder for this preprint (which was not certified by peer review) is the author/funder, who has granted bioRxiv a license to display the preprint in perpetuity. It is made available under aCC-BY 4.0 International license.

Figure 4 – figure supplement 1

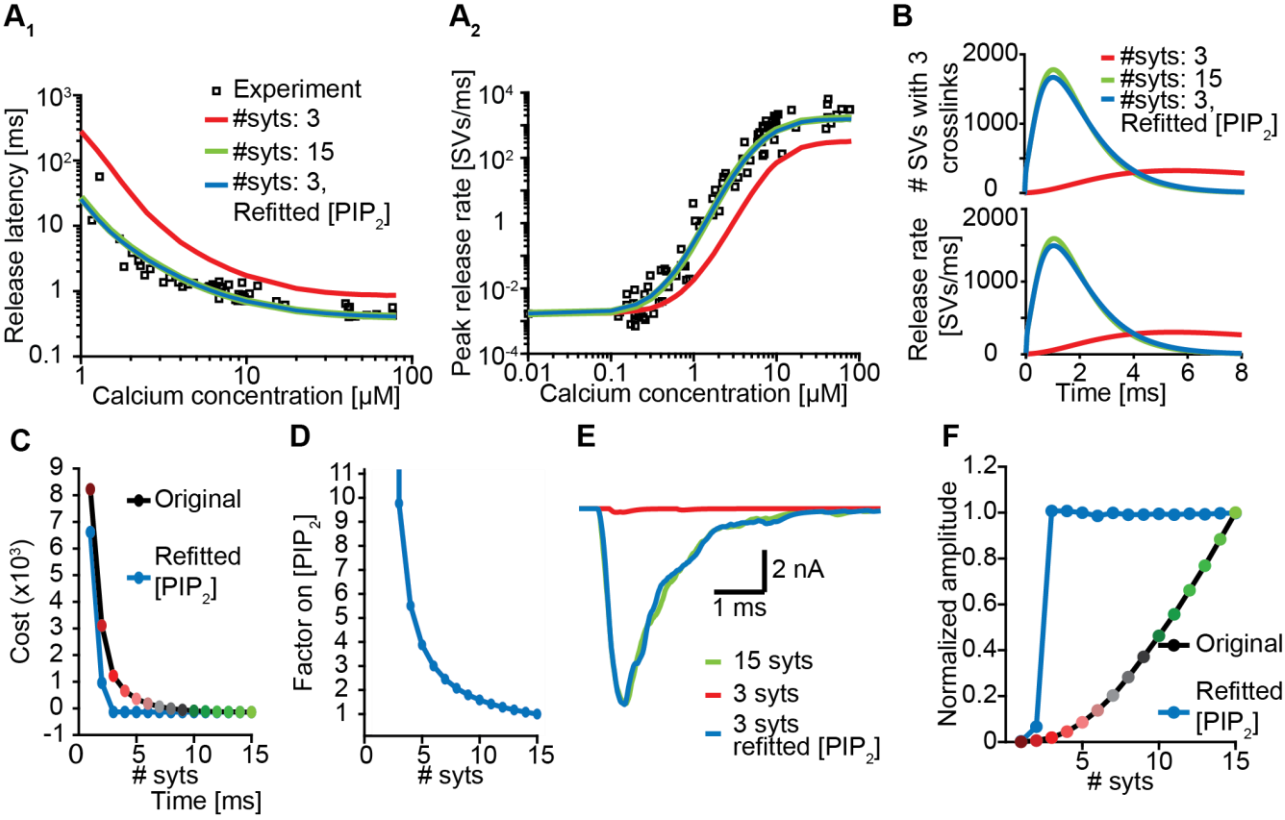

Figure 4 – figure supplement 1. Upregulation of PI(4,5)P_2 can compensate for loss of syts A) Release latencies (A_1) and peak release rates (A_2) for a model with 15 syts (green) and with 3 syts before (red) and after (blue) refitting of [PI(4,5)P_2]. Experimental data points in panels A are replotted from Kochubey and Schneggenburger (2011).**B)** The average number of SVs with three crosslinks formed (top) and the corresponding release rates (bottom) as a function of time upon stimulation with a Ca^{2+}-flash of 50 µM for a model with 15 syts (green), and with 3 syts before (red) and after (blue) refitting of [PI(4,5)P_2]. **C)** The costs values associated with the Ca^{2+}-uncaging data for different levels of syt with the original best fit parameters (black line) and after re-fitting [PI(4,5)P_2] for each choice of n_{syts} (blue line). **D)** The fold-increase in [PI(4,5)P_2] obtained by re-fitting the model as a function of the number of syts**. E)** Representative AP-evoked response of a model with 3 syts per SV obtained after increasing [PI(4,5)P_2] plotted together with representative responses for a model with 3 and 15 syts with the original [PI(4,5)P_2]. **F)** Average amplitudes of simulated AP-evoked responses at original [PI(4,5)P_2] and using the increased values.

bioRxiv preprint doi: https://doi.org/10.1101/2021.10.22.465434; this version posted October 23, 2021. The copyright holder for this preprint (which was not certified by peer review) is the author/funder, who has granted bioRxiv a license to display the preprint in perpetuity. It is made available under aCC-BY 4.0 International license.

Figure 5 – figure supplement 1

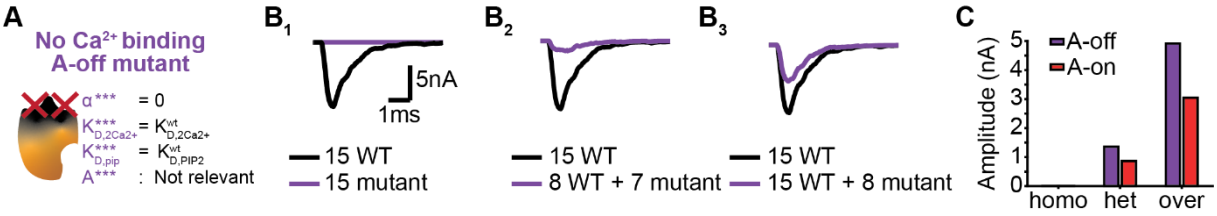

Figure 5 – figure supplement 1. The dominant negative effect of a mutant that is unable to bind Ca^{2+} depend on whether the mutation affects $PI(4,5)P_2$-binding affinities. A) Schematic illustration of the "*No Ca^{2+}-binding, A-off*" mutant, which is not able to bind Ca^{2+} implying that the allosteric interaction between Ca^{2+} and $PI(4,5)P_2$ is always 'inactive'. **B)** Representative, stochastically simulated AP-responses with homozygous (left, 15 mutants), heterozygous (middle, 7 mutants + 8 WT) and overexpression (right, 8 mutants +15 WT) of the A-off mutant. For each of the examples representative trace of a condition with 15 WT syts is shown in black. **C)** Comparison of the mean amplitudes of AP-evoked responses (n=200) simulated with "*No Ca^{2+}-binding, A-off*" mutant to the mean amplitudes of the "*No Ca^{2+}-binding, A-on*" mutant (Figure 5).

bioRxiv preprint doi: https://doi.org/10.1101/2021.10.22.465434; this version posted October 23, 2021. The copyright holder for this preprint (which was not certified by peer review) is the author/funder, who has granted bioRxiv a license to display the preprint in perpetuity. It is made available under aCC-BY 4.0 International license.

Figure 5 – figure supplement 2

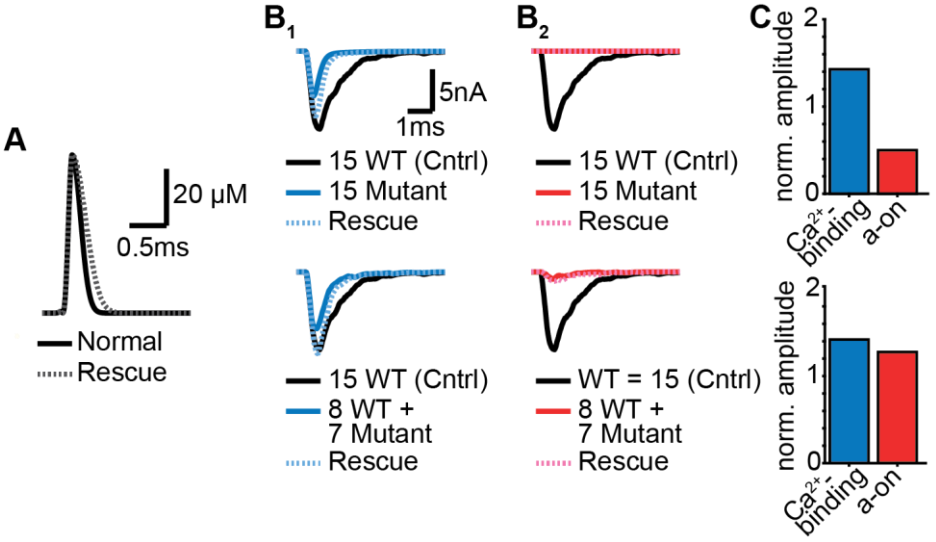

Figure 5 – figure supplement 2. AP-evoked responses of only the Ca^{2+}-binding mutant can be rescued by increased Ca^{2+} influx. A) Ca^{2+} transient with slower decay kinetics (dotted line) and the original Ca^{2+} signal (solid line, (Wang *et al.*, 2008)). **B**) AP-evoked EPSCs simulated using the broader Ca^{2+} signal (dotted line) for homozygous (15 mutants, top) and heterozygous (7 mutants and 8 WT protein, bottom) with the "Ca^{2+}-binding" (B_1) and "no-Ca^{2+}, A-on" mutant (B_2). For each setting a representative trace of a condition with 15 WT syts is shown in black. **C)** Mean amplitudes of eEPSCs simulated with the broader Ca^{2+} signal normalized to the amplitudes obtained with the original Ca^{2+} signal for homozygous (top) and heterozygous (bottom) expression of the mutant (n=200).